Mon. Not. R. Astron. Soc. **000**, 1–32 (2005) Printed 9 July 2007 (MN LATEX style file v2.2)

A *Chandra* X-ray survey of nearby dwarf starburst galaxies: I. Data reduction and results

Jürgen Ott[1⋆], Fabian Walter[2]†, and Elias Brinks‡[3,4]
[1] *CSIRO Australia Telescope National Facility, Cnr Vimiera & Pembroke Roads, Marsfield NSW 2112, Australia*
[2] *Max–Planck–Institut für Astronomie, Königstuhl 17, 69117 Heidelberg, Germany*
[3] *Instituto Nacional de Astrofísica Óptica y Electrónica, Apartado Postal 51 y 216, Puebla, Pue 72000, Mexico*
[4] *Centre for Astrophysics Research, University of Hertfordshire, College Lane, Hatfield AL10 9AB, England*

9 July 2007

ABSTRACT

We present an analysis of *Chandra* X-ray observations of a sample of eight dwarf starburst galaxies (I Zw 18, VII Zw 403, NGC 1569, NGC 3077, NGC 4214, NGC 4449, NGC 5253, and He 2–10). Extended, diffuse X-ray emission is detected in all but two of the objects. Unresolved sources were found within all dwarf galaxies (total: 55 sources). These point sources are well fit by power law, thermal plasma, or black body models. Ten of the point sources exceed an X-ray luminosity of 10^{39} erg s^{-1} (ultraluminous X-ray sources). In those galaxies where diffuse X-ray emission is detected, this emission (with X-ray luminosities ranging from 4×10^{38} erg s^{-1} to 2×10^{40} erg s^{-1}) contains most (60-80 per cent) of the X-ray photons. This diffuse emission can be well fit by MeKaL one-temperature thermal plasma models once the contribution from the unresolved point sources is subtracted properly. The diffuse X-ray component is significantly extended, reaching as far as $0.5 - 5$ kpc into the outskirts of their hosts. Azimuthally averaged X-ray surface brightness profiles are well approximated by exponential functions. Temperatures of various regions within the galaxies range from $1.6 - 7.6 \times 10^6$ K. With few exceptions, temperatures of the hot gas are remarkably uniform, hovering around $2 - 3 \times 10^6$ K. Temperatures of the coronal gas in the outer regions are in general $\sim 2 - 3$ times lower than those found in the central regions. Fits to the diffuse emission do not allow strong constraints to be put on the metallicities of the emitting plasmas. However, the derived metallicities are compatible with those determined from their H II regions. An α/Fe ratio of ~ 2 is indicated for the hot gas within at least three objects (NGC 1569, NGC 4449, and He 2–10). Shadowing of the diffuse X-ray emission by the cooler disc gas is used to constrain the orientation of the galaxies.

Key words:
ISM: jets and outflows – galaxies: dwarf – galaxies: individual (I Zw 18, VII Zw 403, NGC 1569, NGC 3077, NGC 4214, NGC 4449, NGC 5253, He 2-10) – galaxies: starburst – X-rays: ISM – X-rays: galaxies

1 INTRODUCTION

Feedback from massive stars is a fundamental process regulating the energetics and dynamics of the interstellar medium (ISM; e.g., McKee & Ostriker 1977; Leitherer, Robert, & Drissen 1992; Korpi et al. 1999; Gazol-Patiño & Passot 1999; Wada, Spaans, & Kim 2000). An extreme form of feedback can be observed in starburst galaxies which exhibit star formation (SF) at a level that would consume the total fuel supply of their hosts within a time frame considerably shorter than a Hubble time. A starburst typically involves several thousand stars more massive than $\sim 8\,M_\odot$ which eventually explode as type II supernovae (SNe), each releasing a mechanical energy of $\sim 10^{51}$ erg in to the ISM. Most of this energy is thermalised, and indirectly can be traced by X-ray emission emerging from hot, coronal gas (Weaver et al. 1977; Strickland et al. 2002; Heckman 2002). Theoretically, the influence of a

⋆ Bolton Fellow, E-mail: Juergen.Ott@csiro.au
† E-mail: walter@mpia.de
‡ E-mail: ebrinks@star.herts.ac.uk

starburst on the dynamics of the ISM is expected to be a function of the total mass of the host galaxy. The most dramatic consequences are expected to be visible in dwarf starburst galaxies which may lose part or even all of their metal-enriched gas to the intergalactic medium (see, e.g., Mac Low & Ferrara 1999; Ferrara & Tolstoy 2000; Silich & Tenorio–Tagle 2001; Silich et al. 2001).

In order to understand the impact of a starburst on the ISM of its host in more detail, we analyse archival data of a sample of eight nearby starburst dwarf galaxies obtained with the *Chandra* X-ray observatory. Our study is split into two papers. The description of the data, the data reduction and the results of the X-ray analysis are described in Paper I (this paper). Paper II (Ott, Walter & Brinks 2005) compares the X-ray data, both unresolved and extended emission, with observations at other wavelengths and provides a discussion on the state of the ISM, correlations with star formation tracers, and the development of superwinds which can lead to outflows.

Some of the galaxies analysed here have recently been published as individual studies (NGC 3077: Ott, Martin & Walter 2003; NGC 1569: Martin, Kobulnicky & Heckman 2002; NGC 4449: Summers et al. 2003; NGC 4214 Hartwell et al. 2004; I Zw 18: Thuan et al. 2004). Our new analysis, however, is unique in the sense that it provides *uniformly reduced datasets* which allow a direct comparison of the properties of different dwarf galaxies. This is particularly important as results from the analysis of X-ray data critically depend on the binning of the data, the choice of models used for the spectral fits, and in a subtle way on a host of additional variables, such as the proper subtraction of unresolved sources and the way absorption within the object as well as foreground absorption by the Milky Way is dealt with. The aim of our papers is to provide the best analysis possible given our current knowledge and techniques and, in case some systematic effects remain, be able to at least compare results among objects which have been reduced in the same manner.

In Sect. 2 we describe the sample selection criteria followed by a description of the data reduction techniques used for our analysis. The results for the individual galaxies are presented in Sections 3 (galaxies without a detected diffuse X-ray component) and 4 (galaxies with extended X-ray emission). A summary is provided in Sect. 5.

2 *CHANDRA* OBSERVATIONS AND DATA REDUCTION

2.1 Sample selection

As mentioned in the introduction, the effect of a starburst on small galaxies is expected to be far more devastating than the impact a similar such event would have if it takes place within a larger system. We therefore decided to concentrate our efforts on dwarf starburst galaxies. To obtain a sample of galaxies, we searched the *Chandra* archive for data on actively star forming dwarf galaxies which were publicly available by November 2002. Only data collected by the ACIS-S3 CCD were selected as this detector has a high quantum efficiency (~ 0.8 at 1 keV), high spectral resolution (~ 120 eV), high angular resolution ($\sim 1''$), and a low charge transfer inefficiency. Given the faint nature of dwarf galaxies, observations with integration times less than 10 ks were discarded.

In total, eight *Chandra* observations of dwarf starburst galaxies met the selection criteria mentioned above. These targets are: I Zw 18, VII Zw 403, NGC 1569, NGC 3077, NGC 4214, NGC 4449, NGC 5253, and He 2-10. None of the galaxies in the sample is a member of the Local Group; they fall within a distance range of $2 - 13$ Mpc. Note that all objects were previously detected in X-ray emission by *ROSAT*.

The parameters of the *Chandra* observations of the galaxies in our sample are listed in Table 1. In Columns 2 and 3, the coordinates of each object are given. Columns 4 and 5 list the Observation IDs and the Sequence numbers of the corresponding entry in the *Chandra* archive, respectively. The observation dates are displayed in Column 6. Column 7 shows the total exposure time $t_{\rm exp}$. The focal plane temperatures $T_{\rm fp}$ are listed in Column 8 and the pipeline products version numbers in Column 9.

2.2 Data preparation and imaging

For all datasets the satellite telemetries were processed at the *Chandra X-ray Center* (CXC) with the Standard Data Processing (SDP) system, to correct for the motion of the satellite and to apply instrument calibration. Order-sorting/Integrated Probability Tables were applied to all observations using CALDB v.2.9. All data products were analysed with the CXC *Chandra* Interactive Analysis of Observations (CIAO, v.2.2) software, including Data Model tools and the fitting software Sherpa. According to the CXC[1], the pointing accuracy of the observations is $1''$ for each observation. Times of intermittent strong background rates were discarded at levels higher than 3σ of the quiescent periods.

Broad X-ray bands were constructed in order to separate oxygen line complexes (*soft band (S):* $0.3\,{\rm keV} \leqslant E \leqslant 0.7\,{\rm keV}$) from Fe-L lines (*medium band (M):* $0.7\,{\rm keV} \leqslant E \leqslant 1.1\,{\rm keV}$) and the relatively line-free continuum emission (*hard band (H):* $1.1\,{\rm keV} \leqslant E \leqslant 6.0\,{\rm keV}$). Also, the sum of the bands (*total band:* $0.3\,{\rm keV} \leqslant E \leqslant 6.0\,{\rm keV}$) was analysed. For the purpose of imaging we applied the corresponding bad pixel masks (provided by the CXC) and exposure maps. We also constructed hardness ratios[2] which are defined as

$$\begin{aligned} HR1 &= (S-M-H)/(S+M+H) \quad \text{and} \\ HR2 &= (S+M-H)/(S+M+H). \end{aligned} \tag{1}$$

In Table 2 we show the resulting 3σ detection limits for all bands (Columns 2–5). The remaining exposure time $t_{\rm eff}$ after removing the background flaring is given in Column 6.

The deepest observations were performed on NGC 1569 ($t_{\rm eff} = 75$ ks). With a distance of only 2.2 Mpc it is also the nearest galaxy in the sample and therefore provides the best opportunity to explore the properties of the hot gas (see

[1] see *http://cxc.harvard.edu/cal/ASPECT/celmon/index.html*

[2] Here we use a three-band definition which has the advantage of being meaningful even in those cases where emission is present in only one band.

Table 1. Parameters of the *Chandra* observations. Coordinates are given in J2000.

Galaxy	Right Ascension $h\ m\ s$	Declination $\circ\ \prime\ \prime\prime$	Obs ID.	Seq. No.	Date	$t_{\rm exp}$ [ks]	$T_{\rm fp}$ [°C]	ASCDS Ver.
(1)	(2)	(3)	(4)	(5)	(6)	(7)	(8)	(9)
I Zw 18	09 34 02.00	55 14 28.0	805	600108	2000 Feb 8	41.3	−120	R4CU5UPD11.2
VII Zw 403	11 28 01.30	78 59 34.6	871	700176	2000 Jan 7	10.6	−110	R4CU5UPD11.1
NGC 1569	04 30 49.00	64 50 54.0	782	600085	2000 Apr 11	97.1	−120	R4CU5UPD13.1
NGC 3077	10 03 20.66	68 44 03.5	2076	600210	2001 Mar 7	54.1	−120	R4CU5UPD14.1
NGC 4214	12 15 38.70	36 19 41.9	2030	600164	2001 Oct 16	26.8	−120	DS6.3.1
NGC 4449	12 28 12.00	44 05 41.0	2031	600165	2001 Feb 4	26.9	−120	R4CU5UPD14.1
NGC 5253	13 39 56.00	−31 38 24.4	2032	600166	2001 Jan 13	57.4	−120	R4CU5UPD13.3
He 2-10	08 36 15.15	−26 24 34.0	2075	600209	2001 Mar 23	20.0	−120	R4CU5UPD14.1

Table 2. 3σ detection limits in the different bands (given as flux count rates in units of 10^{-8} cts $\rm s^{-1}\,cm^{-2}$). The last column lists the effective exposure times of the *Chandra* observations in ks.

Galaxy	Soft	Medium	Hard	Total	$t_{\rm eff}$
(1)	(2)	(3)	(4)	(5)	(6)
I Zw 18	2.0	0.8	2.8	2.4	18.3
VII Zw 403	2.3	1.1	4.0	3.2	10.5
NGC 1569	0.9	0.4	1.4	1.2	75.0
NGC 3077	1.2	0.5	1.8	1.4	53.2
NGC 4214	2.6	1.2	3.3	2.8	11.4
NGC 4449	1.9	0.6	2.1	1.9	31.0
NGC 5253	0.9	0.7	2.3	1.9	44.3
He 2-10	1.9	0.7	2.5	2.2	20.0

Martin, Kobulnicky & Heckman 2002). The observation of VII Zw 403 has the shortest $t_{\rm eff}$ and the highest focal point temperature. The detection limits of VII Zw 403 are therefore the highest of our sample.

For each galaxy, we separately study the point source population and the purely diffuse emission. Two CIAO source detection algorithms WAVDETECT and CELLDETECT were applied for the identification of the point sources using the total band X-ray image. The degradation of the point spread function (PSF) at large off-axis angles was taken into account by applying scales of $0\farcs5$, $1\farcs0$, and $2\farcs0$ wavelet radii in WAVDETECT. For CELLDETECT we used S/N ratios of 1.9, 2.1, and 3.2 within off-axis radii r of $0' < r < 1'$, $1' < r < 2\farcm5$, and $2\farcm5 < r < 3\farcm5$, respectively. Beyond a radius of $3\farcm5$ the PSF is too degraded to provide reliable CELLDETECT detections.

Only those point sources were considered which were detected within the general area covered by the Hα, optical or diffuse X-ray emission of the galaxies under study. All point sources are treated in this paper as if they reside within the targets. Interlopers, such as stars in the Milky Way or background active galactic nuclei (AGN) may be visible as less absorbed, extremely soft or highly absorbed, hard X-ray point sources, respectively. In particular, those point sources which are best-fitted by power law models with an index of about 1.4 (cf. the Chandra Deep Field observations, Tozzi et al. 2001) and with large absorbing column densities (due to the dwarf galaxies and the Galaxy) might be distant AGNs.

In order to obtain images of the diffuse X-ray emission, point sources over an area corresponding to three times the point spread function (PSF) were blanked from the data. These areas were subsequently refilled by interpolated count rates from the ambient diffuse X-ray emission. As a result we obtained purely diffuse X-ray maps in the different energy bands. The count rates of the X-ray data with and without point sources are listed in Table 3.

In addition to the raw pixel maps, all maps were adaptively smoothed (task CSMOOTH) with a lower and an upper S/N of 3 and 4, respectively, using a fast Fourier method. The corresponding exposure maps were smoothed as well, using the same smoothing kernels as computed for the respective images. Smoothed images, however, were not used for any quantitative analyses but for visualisation purposes only.

2.3 Spectral analysis

In addition to broad band images, we derived spectra of the discrete and diffuse X-ray emission of the galaxies in our sample (energy range: $0.3\,{\rm keV} \leqslant E \leqslant 8.0\,{\rm keV}$). For this purpose, we used CALDB v.2.9 to calibrate the data. REDISTRIBUTION MATRIX FILES (RMFs) and AUXILIARY RESPONSE FILES (ARFs) were constructed for the central positions of the apertures from which corresponding spectra where extracted.

Finally, the consecutive *pulse-invariant* (PI) channels were binned by a factor of three. This still left the spectra sufficiently oversampled as the energy width of a single PI channel is 14.6 eV whereas the spectral resolution of the ACIS-S3 chip at 1 keV is ~ 120 eV. The spectra were eventually fitted by different models within the SHERPA v.2.2 software. The models were convolved with the appropriate RMFs and ARFs and we used the χ^2 Gehrels statistics (Gehrels 1986). This statistics is designed to work with low numbers (accuracy: $\sim 1\%$) and also permits background subtraction as well as the assessment of the quality of a fit via the goodness–of–fit χ^2 indicator. To obtain the parameters which best describe the data we used a Monte-Carlo fitting technique which randomly defines 20 starting values within a physically sensible parameter space followed by the single-shot Powell optimisation method to derive the final set of parameters (*Monte-Powell* in SHERPA). The apertures for point sources are sufficiently small to allow the background contribution to be neglected ($\sim 1-5$ counts). The larger apertures used for diffuse emission, however, do contain significant background emission. This emission was subtracted using spectra from regions with similar CCD rows as the source regions.

For all models we fixed the absorbing Galactic fore-

Table 3. X-ray count rates of galaxies where diffuse X-ray emission is detected. For each band the count rates are given in units of 10^{-3} cts s^{-1}.

Band	NGC 1569	NGC 3077	NGC 4214	NGC 4449	NGC 5253	He2-10
			X-Ray Emission Including Point Sources			
Total	112.16 ± 1.64	21.73 ± 0.94	59.82 ± 2.65	361.55 ± 4.18	38.57 ± 1.08	69.49 ± 2.03
Soft	13.66 ± 0.68	5.22 ± 0.47	13.13 ± 1.30	97.11 ± 2.23	8.57 ± 0.53	10.17 ± 0.85
Medium	53.17 ± 0.94	9.02 ± 0.47	18.41 ± 1.39	133.46 ± 2.33	19.88 ± 0.66	34.62 ± 1.34
Hard	45.33 ± 1.16	7.49 ± 0.67	28.28 ± 1.85	130.72 ± 2.65	10.12 ± 0.67	24.70 ± 1.26
			Diffuse X-Ray Emission Only			
Total	75.95 ± 1.48	13.96 ± 0.86	23.44 ± 1.95	174.70 ± 3.23	26.45 ± 0.96	45.40 ± 1.70
Soft	10.49 ± 0.65	4.25 ± 0.45	9.52 ± 1.17	68.27 ± 1.98	6.66 ± 0.50	7.90 ± 0.78
Medium	41.35 ± 0.85	7.62 ± 0.44	8.90 ± 1.05	81.47 ± 1.87	14.67 ± 0.57	27.74 ± 1.21
Hard	23.96 ± 1.03	1.83 ± 0.59	4.93 ± 1.16	23.20 ± 1.73	5.02 ± 0.59	9.46 ± 0.90

ground column density to the measurements of atomic neutral hydrogen (H I) performed by Hartman & Burton (1997) (listed in Table 4). A solar metallicity and element mixture was assigned to this absorbing gas (model XSPHABS, Balucinska–Church & McCammon 1992; abundances taken from Anders & Grevesse 1989). In addition, we used a second absorption component with a metal abundance corresponding to the internal metallicity of the objects (based on H II region oxygen abundances, see Table 4 – for a justification see Sect. 4). The data were not corrected for molecular contamination of the ACIS optical blocking filter which may introduce another $3 - 7 \times 10^{20}$ cm^{-2} of absorbing column with solar metallicity, dependent on the observing dates. The resulting model expressions for Sherpa are: $model = xsphabs(Galactic) \times xsvphabs(internal) \times EMITTER$, where $EMITTER$ stands for the emission model, e.g., PLAW1D (power law, PL), BLACK (black body, BB), XSBREMSS (thermal bremsstrahlung, Brems), XSMEKAL (MeKaL thermal plasma model; Mewe, Gronenschild & van den Oord 1985; Kaastra 1992; Liedahl, Osterheld & Goldstein 1995). The normalisations are given as: $10^{-14}(4\pi D^2)^{-1} \int n_e n_H dV$ (MeKaL) and $3.02 \times 10^{-15}(4\pi D^2)^{-1} \int n_e n_I dV$ (Brems) where D is the distance to the source in cm, n_e, n_H, and n_I are the electron, proton, and ion densities respectively, and V the volume of the emission region. The BB model amplitude is given as $2\pi\,(c^2h^3)^{-1}(R/D)^2 = 9.884 \times 10^{31}(R/D)^2$ (R: radius of the object; the speed of light, c, is given in cm s^{-1}, and the Planck constant, h, is specified in keV s). The normalisation reference point for the PL model was set to 1 keV. Confidence regions for the individual fits were produced using the *region–projection* task in SHERPA. Whenever the confidence levels are computed in a plane defined by two parameters, *region–projection* still allows all the other free parameters to vary, i.e., they are not frozen to the values of the best fit.

3 GALAXIES WITHOUT DIFFUSE X-RAY EMISSION

For two galaxies of our sample, I Zw 18 and VII Zw 403, we did not detect diffuse X-ray emission. Instead, we calculated upper limits based on the sizes of their optical bodies. To do so, we simulated absorbed thermal plasma emission from hot gas that we would be able to detect. The temperature of the thermal plasma is assumed to be 0.2 keV (equivalent to 2.3×10^6 K) with a metallicity corresponding to that measured in their H II regions (see Table 4). This hot gas temperature is similar to that derived by spectral fitting of the other galaxies in the sample (cf. Sect. 4). We also assumed photoelectric absorption by gas local to the dwarf starburst galaxy with a canonical column density of $N_H = 1.5 \times 10^{21}$ cm^{-2} (see Sect. 2.3 for details). Finally, we adjusted the normalisation of the plasma models in a way such that the peaks of the spectra were at just $\sim 2\sigma$ of the measured background counts, but visible in ~ 5 channels. This leads to upper limits of the diffuse X-ray fluxes and luminosities which are summarised in Table 5. The results for the discrete X-ray emission of I Zw 18 and VII Zw 403 are as follows.

Table 5. Sensitivity limits of the *Chandra* observations for hot gas in galaxies, where no diffuse emission is detected (I Zw 18 and VII Zw 403). The internal absorbing column density is fixed to 1.5×10^{21} cm^{-2} and the plasma temperature to 0.2 keV ($\simeq 2.3 \times 10^6$ K). Absorbed ($F_X^{abs}[0.3-8.0\,\mathrm{keV}]$) and absorption corrected (F_X) fluxes are given in units of 10^{-15} erg s^{-1} cm^{-2} and luminosities (L_X) in 10^{37} erg s^{-1}.

Galaxy	F_X^{abs}	F_X	L_X
I Zw 18	9	20	37
VII Zw 403	33	120	28

3.1 I Zw 18 (Mrk 116, UGCA 166)

3.1.0.1 Previous X-ray observations and results

ROSAT PSPC data (17 ks) of I Zw 18 were analysed by Martin (1996). They reported the detection of a point source with a luminosity of $\sim 10^{39}$ erg s^{-1} and explained its nature partly with hot thermal gas. Faint, diffuse extensions of this source are reported by Bomans (2001), based on *ROSAT* HRI observations (64 ks), as well as by Bomans & Weis (2002) and Thuan et al. (2004) based on the same *Chandra* data as presented here. Thuan et al. (2004) derive the 0.5–10.0 keV X-ray luminosity of this point source to either 1.6×10^{39} erg s^{-1}or 1.4×10^{39} erg s^{-1} depending on whether a PL or an Raymond–Smith (RS; Raymond & Smith 1977) thermal plasma model is applied.

Table 4. Distances, oxygen abundances $12 + \log(O/H)$, the corresponding metallicities Z (relative to solar abundances), and Galactic H I foreground column densities $N_{\rm H}^{\rm Gal}$ of the sample ($N_{\rm H}^{\rm Gal}$ taken from Hartman & Burton 1997).

Galaxy	Distance [Mpc]	$12 + \log(O/H)$	Z [solar]	$N_{\rm H}^{\rm Gal}$ [10^{20} cm^{-2}]	Reference cols 2, 3
(1)	(2)	(3)	(4)	(5)	(6)
I Zw 18	12.6	7.16	0.02	2	1, 2
VII Zw 403	4.5	7.73 ± 0.01	0.07	3	3, 4
NGC 1569	2.2	8.22 ± 0.07	0.21	12	5, 6
NGC 3077	3.6	8.90	1.00	4	7, 6
NGC 4214	2.9	8.28 ± 0.08	0.25	3	8, 9
NGC 4449	3.9	8.31 ± 0.07	0.26	1	10, 6
NGC 5253	3.3	8.23 ± 0.01	0.21	5	11, 6
He 2-10	9.0	8.93	1.07	9	12, 13

References: (1) Östlin (2000); (2) Guseva, Izotov & Thuan (2000); (3) Lynds et al. (1998); (4) Izotov, Thuan & Lipovetsky (1997); (5) Israel (1988); (6) Martin (1997); (7) Freedman et al. (1994); (8) Maíz-Apellániz, Cieza & MacKenty (2002); (9) Kobulnicky & Skillman (1996); (10) Hunter et al. (1998); (11) Gibson et al. (2000); (12) Vacca & Conti (1992); (13) Kobulnicky, Kennicutt & Pizagno (1999)

Table 6. Coordinates, net source counts and hardness ratios of the X-ray point sources in I Zw 18 and VII Zw 403. The source counts are given in 10^{-3} cts s^{-1}.

	I Zw 18	VII Zw 403
Right Ascension (J2000)	$09^h34^m01\overset{s}{.}9$	$11^h28^m03\overset{s}{.}0$
Declination (J2000)	$55°14'28\overset{''}{.}4$	$78°59'53\overset{''}{.}3$
Soft	3.22 ± 0.42	7.53 ± 0.90
Medium	4.04 ± 0.47	6.31 ± 0.81
Hard	5.25 ± 0.57	14.55 ± 1.24
Total	12.51 ± 0.85	28.40 ± 1.74
HR1	-0.49 ± 0.08	-0.47 ± 0.06
HR2	0.16 ± 0.07	-0.03 ± 0.06

3.1.0.2 *Chandra* **observations revisited** In addition to five background sources in the ACIS-S3 field of view, the *Chandra* observations show a source coinciding with the optical counterpart of I Zw 18 (see Fig. 1, upper left). This source is located on the rim of a central expanding Hα superbubble (described by Martin 1996), north-west to the main optical body. Based on the *HST*/WFPC2 data shown in Fig. 1, no stellar counterpart can be assigned to this X-ray point source.

We checked whether or not the source may be slightly extended by comparing its shape with a model PSF calculated for the same off-axis angle and the same mean energy as the X-ray source itself. According to our analysis, the PSF and the X-ray source profiles are indistinguishable. We do not find evidence for excess emission towards the extensions claimed by Bomans & Weis (2002) and Thuan et al. (2004).

Coordinates, net source counts in the different bands, and hardness ratios of the point source are listed in Table 6. In addition, we extracted a source spectrum, which is displayed in Fig. 1 (lower left). The spectrum peaks at $\sim$ 0.6 keV with a steep decline to softer energies and a shallower decline to harder energies. We decided to fit four models to the spectrum: (a) PL, (b) BB, (c) Brems, and (d) MeKaL. The results are summarised in Table 7. Overlays of these models on the spectrum are shown in Fig. 1. All models provide reasonable fits to the data and their $\chi^2_{\rm red}$ are very similar, in the range of 0.12 (PL fit) to 0.14 (BB fit). The X-ray luminosity of the models range from $\sim 1.0 - 5.2 \times 10^{39}$ erg s^{-1}, which is in good agreement with previous results. This source falls within the class of ultra-luminous X-ray sources (ULXs, defined as sources having $L_{\rm X} > 10^{39}$ erg s^{-1}).

In what follows we will try to derive which of the models best describes the point source. A PL model would indicate that the source is likely an X-ray binary (XRB). With a power law photon index of 3.3, however, it exhibits a very steep spectrum. The Eddington limit of a source is given by $L_{\rm E} = 1.3 \times 10^{38} (M/M_\odot)$ erg s^{-1}. If a source exceeds this limit stable accretion is not possible anymore; the force from radiation pressure exceeds the force needed to overcome the gravitational potential. If the accreting object in the XRB has a mass lower than $\sim 40\,{\rm M}_\odot$ (PL luminosity of the X-ray point source in I Zw 18: $L_{\rm X} = 5.2 \times 10^{39}$ erg s^{-1}), it is above the Eddington threshold. This would indicate the presence of a super Eddington source which would imply that the source should be variable in time. We therefore checked the point source in I Zw 18 for possible variability within the observational time frame. To do so, we binned its spectrum in 60, 200, 600, and 1000 s time bins and constructed the corresponding light curves. The light curves do not suggest temporal variability on the time scales given by the binning and the length of the observation.

Black body radiation can be emitted by a single star, a helium burning white dwarf, or an isolated neutron star. The fitted temperatures and luminosities, however, are too high for any of these objects.

Alternatively, a collisional thermal plasma can be responsible for the measured spectrum. In addition to the continuum emission (modeled by thermal bremsstrahlung), line transitions might still play a role which are described, e.g., by the MeKaL code (which also includes the bremsstrahlung component). The bremsstrahlung model results in a higher absorbing column density and a lower temperature as compared to the MeKaL fits. For temperatures higher than $\sim 10^7$ K, both models should provide the same results, as line radiation is not a dominant contribution to the X-ray emission anymore (see Sutherland & Dopita 1993). For lower temperatures, MeKaL models are more appropriate as compared to pure thermal bremsstrahlung. If the thermal plasma scenario for the point source in I Zw 18 is realistic, then its nature is probably a (young) supernova remnant (SNR). However, the X-ray luminosity of this source is probably too large for this option to be a viable one. Blair & Long (2004), e.g., show that in M 83 the maximum

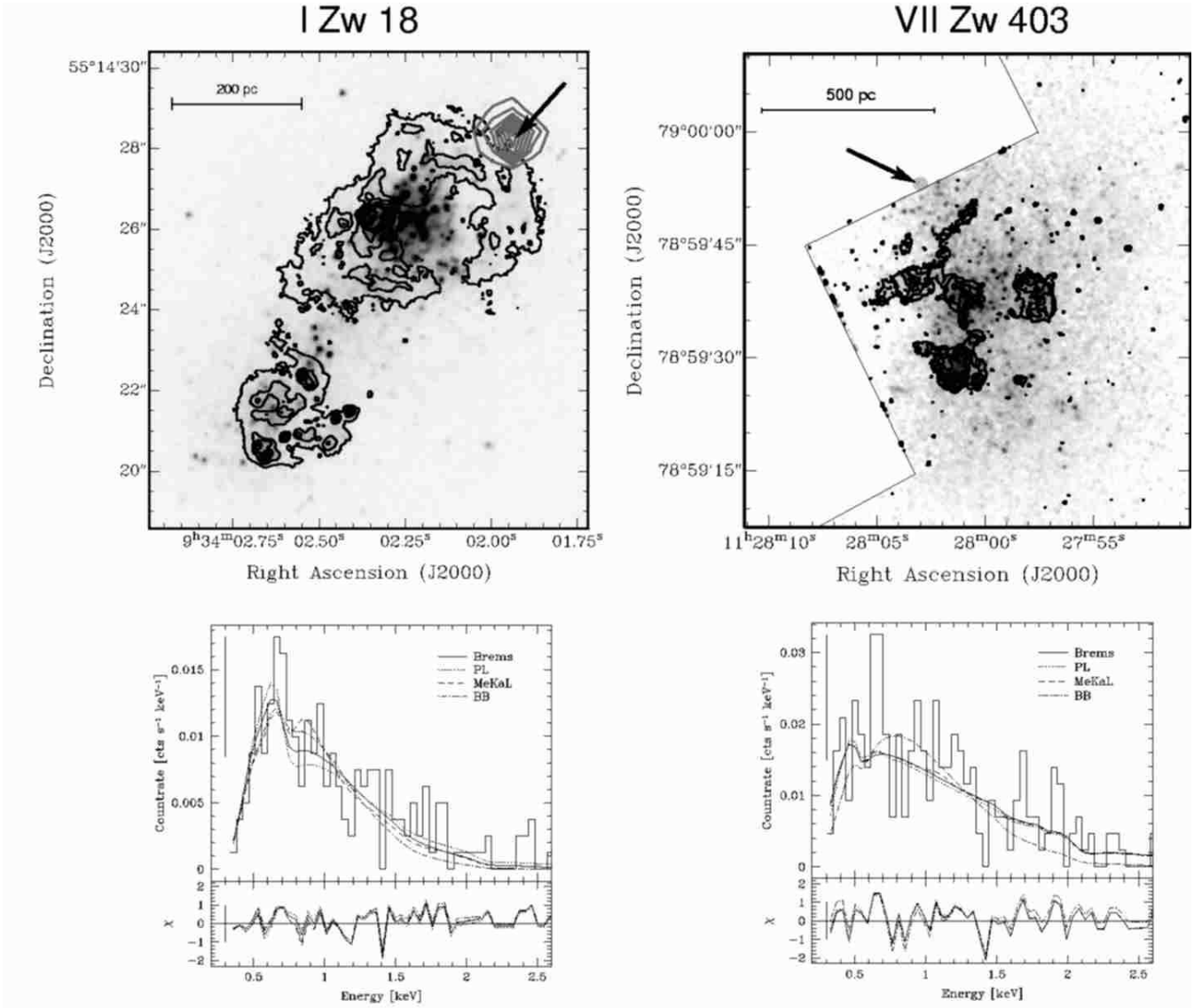

Figure 1. Images and X-ray spectra of I Zw 18 (**left hand panels**) and VII Zw 403 (**right hand panels**). Displayed are *HST*/WFPC2 images of I Zw 18 and VII Zw403 in the F675W and F555W bands, respectively (**top**). Hα emission is shown as **black contours**; the **grey contours** display the locations of the X-ray point sources (also marked by the arrows). Note that the X-ray point source in VII Zw 403 is right at the border of the WFPC2 PC CCD (borders marked by the thin black line). The lower panels show the spectra of the respective point sources as histograms with the fit results of each model overlaid (**Brems**: thermal bremsstrahlung, **PL**: power law, **MeKaL**: MeKaL thermal plasma, **BB**: black body). The typical errors of the spectra are plotted in the upper left corners. The lower portions of these graphs display the errors $\chi = (Data - Model)/Error$ of the corresponding models with the errorbar to the left. A large $|\chi|$ indicates a bad fit and the optimum is reached for $|\chi| \sim 1$ (optical images of I Zw 18 taken from Cannon et al. 2002).

X-ray luminosity of an SNR does not exceed $\sim 10^{37}$ erg s^{-1}, which is about two orders of magnitude lower than what we derive for the point source in I Zw 18.

The source is located on the rim of the Hα superbubble (Fig. 1, upper left). It may therefore have formed as a result of induced star formation on the expanding shell which in turn has probably its origin in the central stellar population seen in optical bands. Given the extreme luminosity and small size of this object, we will prefer the XRB scenario and adopt this for our analysis presented in Paper II.

3.2 VII Zw 403 (UGC 6456)

3.2.0.3 Previous X-ray observations and results Papaderos et al. (1994) analysed *ROSAT* PSPC (10 ks) observations of VII Zw 403. They detected a point-like source with some extended faint structures. The total X-ray luminosity of this object was derived to be 1.9×10^{38} erg s^{-1}.

3.2.0.4 *Chandra* **observations** The ACIS-S3 *Chandra* observations of VII Zw 403 were performed with an integration time of $\sim$ 10 ks. One unresolved X-ray source is detected to coincide with the optical body of VII Zw 403 (see the upper right panel of Fig. 1 for an overlay, and Ta-

Table 7. Fits to the point sources in I Zw 18 and VII Zw403. Models are abbreviated as in Fig. 1. The parameters are: $N_{\rm H}$: internal absorbing column density, γ: PL photon index, T: temperature, $F_{\rm X}^{\rm abs}$: absorbed X-ray flux ($0.3-8.0$ keV), $F_{\rm X}$: unabsorbed X-ray flux, $L_{\rm X}$: unabsorbed X-ray luminosity, and $\chi^2_{\rm red}$: the reduced χ^2 goodness-of-fit parameter. Note that γ is only applicable for the PL model; the normalisation is given for Brems and MeKaL model fits, whereas the amplitude is used for the PL and BB models. Errors are given for 68.3 per cent confidence.

Parameter	Units	PL	BB	Brems	MeKaL
		I Zw 18			
$N_{\rm H}$	$[10^{21}\,{\rm cm}^{-2}]$	$15.04^{+5.95}_{-6.19}$	$6.24^{+5.09}_{-5.10}$	$10.45^{+4.96}_{-4.93}$	$8.94^{+3.39}_{-3.32}$
γ/T	[–]/[10^6 K]	$3.40^{+0.76}_{-0.76}$	$2.37^{+0.56}_{-0.64}$	$6.75^{+2.20}_{-2.20}$	$7.35^{+1.65}_{-1.64}$
$Ampl/Norm^a$	$[10^{-5}]$	$3.09^{+1.11}_{-1.12}$	$306.2^{+190.0}_{-192.9}$	$9.36^{+6.82}_{-6.71}$	$18.17^{+7.52}_{-7.57}$
$F_{\rm X}^{\rm abs}$	$[10^{-15}\,{\rm erg\,s^{-1}\,cm^{-2}}]$	$39.40^{+36.5}_{-6.05}$	$25.95^{+138}_{-24.74}$	$30.33^{+79.77}_{-26.14}$	$29.97^{+36.44}_{-20.14}$
$F_{\rm X}$	$[10^{-15}\,{\rm erg\,s^{-1}\,cm^{-2}}]$	275^{+469}_{-160}	$52.44^{+149}_{-47.26}$	$62.61^{+58.51}_{-23.04}$	$84.85^{+52.57}_{-43.85}$
$L_{\rm X}$	$[10^{37}\,{\rm erg\,s^{-1}}]$	523^{+891}_{-304}	$99.63^{+284}_{-89.80}$	202^{+245}_{-164}	161^{+100}_{-83}
$\chi^2_{\rm red}$		0.12	0.14	0.13	0.13
		VII Zw 403			
$N_{\rm H}$	$[10^{21}\,{\rm cm}^{-2}]$	$1.16^{+1.58}_{-1.16}$	$0.00^{+2.08}_{-0.00}$	$0.00^{+0.32}_{-0.00}$	$0.12^{+0.94}_{-0.12}$
γ/T	[–]/[10^6 K]	$1.75^{+0.37}_{-0.34}$	$3.14^{+0.77}_{-0.77}$	$52.4^{+0.1}_{-0.1}$	$44.0^{+0.2}_{-0.2}$
$Ampl/Norm^a$	$[10^{-5}]$	$2.43^{+0.69}_{-0.70}$	$110.9^{+56.8}_{-56.9}$	$3.07^{+0.74}_{-0.85}$	$9.60^{+2.02}_{-2.37}$
$F_{\rm X}^{\rm abs}$	$[10^{-15}\,{\rm erg\,s^{-1}\,cm^{-2}}]$	$151.2^{+147.8}_{-79.9}$	$52.61^{+149.0}_{-46.7}$	$148.7^{+30.9}_{-37.2}$	$118.5^{+26.4}_{-33.8}$
$F_{\rm X}$	$[10^{-15}\,{\rm erg\,s^{-1}\,cm^{-2}}]$	$196.9^{+132.0}_{-65.0}$	$61.9^{+163.7}_{-52.1}$	$148.7^{+35.9}_{-41.3}$	$141.1^{+30.0}_{-35.0}$
$L_{\rm X}$	$[10^{37}\,{\rm erg\,s^{-1}}]$	$47.3^{+31.7}_{-15.6}$	$14.8^{+39.3}_{-12.5}$	$35.7^{+8.6}_{-9.9}$	$33.9^{+7.2}_{-8.4}$
$\chi^2_{\rm red}$		0.20	0.25	0.21	0.21

[a] see Sect. 2.3

ble 6 for coordinates, net source counts, and hardness ratios of the X-ray point source). Comparing our map to available *HST*/WFPC2 data, the X-ray source is located on the edge of the WFPC2 PC CCD, so unfortunately no cross-identification is possible. In contrast to the *ROSAT* observations, we neither find evidence for any extension of the discrete source, nor for any extended, diffuse X-ray emission in VII Zw 403 (the upper limit for diffuse X-ray emission is given in Table 5).

The spectrum of the point source is shown in Fig. 1 (lower right). We fitted the same models to the spectrum as for the point source in I Zw 18, but with 7 per cent solar metallicity and the appropriate Galactic foreground absorption. From a statistical point of view, all models but the black body yield fits with about the same $\chi^2_{\rm red}$ and are virtually indistinguishable (see Table 7). The X-ray luminosities of the fits are in the range of $\sim 1.5-4.7\times10^{38}$ erg s^{-1} and therefore in agreement with the *ROSAT* observations.

The power law index for VII Zw 403 is lower than for I Zw 18 (1.8 compared to 3.4) and falls within the range common for XRBs (see, e.g., Irwin, Athey & Bregman 2003). Thermal plasma models all yield very high temperatures (a factor of 6–7 higher than the source in I Zw 18). Therefore, an XRB is the most likely explanation for this X-ray point source. Lightcurves extracted in the same way as for I Zw 18 do not indicate any variability at the 3σ level in the selected bins.

4 GALAXIES WITH DETECTIONS OF DIFFUSE X-RAY EMISSION

Diffuse X-ray emission is encountered in the *Chandra* data of six galaxies: NGC 1569, NGC 3077, NGC 4241, NGC 4449, NGC 5253, and He 2–10. Before discussing the results for these objects one by one, we first describe in some detail how we analysed the diffuse X-ray component and how we dealt with the X-ray point sources which fall within the optical and/or X-ray extent of each target. After presenting the results on the individual galaxies we justify why we used the metallicities derived from H II regions for our model fitting. Lastly we address the issue of deviations from a solar element mixture of the X–ray emitting gas, in particular a possible excess of α elements over Fe.

4.1 Analysis of the diffuse X-ray emission

Point source identification and subtraction (see Sect. 2.2) is crucial for the analysis of the hot gas. The sum of all individual point sources within one galaxy can not be fitted by a simple function (e.g., PL). This is illustrated in the total,

point source+diffuse X-ray emission spectra of the galaxies (panels [g] of Figs. 3, 5, 7, 9, 11, and 13). However, previous analyses of diffuse X-ray components in galaxies, in particular those based on *ROSAT* data, often do not account for this fact and use a *single* power law model to accommodate for the entire point source population. Incorrect subtraction of the point sources will inevitably lead to a bias in the fit to the extended component, the magnitude and nature of which is hard to predict. This could easily lead one to invoke, for example, two-temperature model fits where in reality a one-temperature fit would do. The importance of properly taking into account the contribution from point sources underscores the need for high angular resolution as provided by the *Chandra* observatory.

Thermal plasma models (see Sect. 2.3 for reduction and fitting techniques) are very successful in describing the diffuse X-ray emission. Several models exist in the literature, such as an RS model. More recent models are MeKaL (Mewe, Gronenschild & van den Oord 1985; Kaastra 1992; Liedahl, Osterheld & Goldstein 1995), APEC (Smith et al. 2001) and CLOUDY (Ferland et al. 1998). We decided to use the MeKaL code for our analysis as it is widely used in the literature and overcomes the shortcomings of the RS code in the treatment of Fe-L lines. Its atomic data also contains fluorescence lines which are not available for the other codes. A detailed comparison of the models is provided on the CXC webpages[3].

The MeKaL models did an excellent job in fitting the X-ray emission after the unresolved sources had been subtracted. The introduction of an additional non-thermal component (e.g., in order to account for faint, unresolved point sources) did not significantly improve the fits. We used a single temperature to model the emission. As it turns out, the temperature of the hot, coronal gas varies over the extent of the targets. This we deal with by defining different regions which are fit independently by one-temperature models. In general, we define a central region (R1) and several regions (R2, R3, ..., Rn) defined by polygons which we collectively refer to as the 'outer regions'. The outer regions were selected upon both the Hα and X-ray morphology of each object.

Multi-temperature models do not improve the goodness of the fits obtained for one-temperature models within an individual, small region. In Figs. 3, 5, 7, 9, 11, and 13 (panels [d] and [e]) these regions are overlaid on Hα and unsmoothed X-ray images (note that for illustration purposes those X-ray images are not point source subtracted; point sources were removed, however, for all further analysis). We also combined some of the regions to study the outskirts of the galaxies. It turns out that a one-temperature plasma fit is acceptable even for the entire diffuse X-ray emission. Multi-temperature fits show one component clearly dominating the emission and all other components to have a very low normalisation, i.e., X-ray emissivity. Those additional components can be neglected (cf. panels [g] and [h] of Figs. 3, 5, 7, 9, 11, and 13, where the single-temperature fits are overlaid on the data).

The results of the fits are listed in Tables 8, 12, 15, 18, 21, and 24. In these tables N_H denotes the internal absorbing column density, T is the temperature of the hot gas, $Norm$ the normalisation, $F_{\rm X}^{\rm abs}$ the absorbed flux $(0.3-8.0\,{\rm keV})$, $F_{\rm X}$ the unabsorbed flux, $L_{\rm X}$ the unabsorbed luminosity $(0.3-8.0\,{\rm keV})$, and χ^2_{red} the reduced χ^2 goodness-of-fit parameter. The fits, residuals, and confidence regions in the $N_H - T$ plane (the normalisation was not fixed in the process) are shown in panels [h] and [i] of Figs. 3, 5, 7, 9, 11, and 13. In all our fits we assumed solar abundances for the absorbing foreground gas from the Milky Way whereas we used metallicities based on independent measurements of the H II regions when modelling the emitting X-ray gas and any absorption internal to the objects under study. This is justified *a posteriori* in Sect. 4.9.

4.2 Analysis of the X-ray Point Sources

In addition to the diffuse X-ray emission, we study the spectral properties of the X-ray point source populations of the different galaxies. As a first step, we extracted the source counts and derived the hardness ratios (see Sect. 2.2). These values are listed in Tables 10, 13, 16, 19, 22, and 25. We follow two approaches for a more detailed analysis of the individual point source spectra: (a) we compare their hardness ratios to MeKaL and PL models and (b) we fit different models (Brems, MeKaL, PL, and BB) to their individual spectra. All models assume a metallicity equal to the H II oxygen abundances of their host galaxies. Finally, we derive the best-fitting model for each point source with sufficient source counts (at least three spectral bins with four counts minimum) based on (a) a visual inspection of the fitted spectra, (b) the goodness-of-fit parameter χ^2_{red}, and (c) the source locations in hardness ratio plots (see Figs. 4, 6, 8, 10, 12, and 14 panels [b] and [c]). The grids which are overlaid in the hardness ratio plots are shown in more detail in Fig. 2. They were calculated by simulating model spectra for a range of thermal plasma and PL models. In the case of a thermal plasma, we used MeKaL models and varied the temperature of the plasma and absorbing foreground column density. For the PL models the PL index and absorbing foreground column density were varied. By applying the ARFs and RMFs of the corresponding observations to the artificial spectra, the data were folded with the ACIS–S3 response. The resulting, convolved spectra were subsequently used to calculate the hardness ratios.

The final selection of the source models (based on the criteria described above) and the corresponding fit parameters are listed in Tables 11, 14, 17, 20, 23, and 26.

As a last step, we combined the fits for the diffuse and the discrete sources and overlay the results on the spatially integrated X-ray spectra of the galaxies (including point sources). These are shown in panels (g) of Figs. 3, 5, 7, 9, 11, and 13.

4.3 NGC 1569 (UGC 3056, Arp 210, VII Zw 16)

4.3.1 Previous X-ray observations and results

The first X-ray detection of NGC 1569 was based on data obtained by *EINSTEIN*. NGC 1569 appeared as an extended soft source with a luminosity of $\sim 10^{39}$ erg s^{-1} (Fabbiano, Feigelson & Zamorani 1982). Follow-up observations with the *ROSAT* HRI (11 ks) led to the detection of

[3] *http://cxc.harvard.edu/atomdb/issues_comparisons.html*

Table 8. Results of MeKaL collisional thermal plasma model fits applied to the X-ray spectra of different regions in NGC 1569 (see panels [d] and [e] in Fig. 3 for the definition of the regions).

Region	$N_{\rm H}$	T	$Norm^a$	$F_{\rm X}^{\rm abs}$	$F_{\rm X}$	$L_{\rm X}$	χ^2_{red}
	$[10^{21}\,{\rm cm}^{-2}]$	$[10^6\,{\rm K}]$	$[10^{-5}]$	$[10^{-15}\,{\rm erg\,s^{-1}\,cm^{-2}}]$	$[10^{-15}\,{\rm erg\,s^{-1}\,cm^{-2}}]$	$[10^{37}\,{\rm erg\,s^{-1}}]$	
Total	$2.86^{+0.15}_{-0.15}$	$7.23^{+0.12}_{-0.12}$	$80.0^{+1.5}_{-1.5}$	205^{+10}_{-10}	721^{+15}_{-15}	$41.7^{+6.0}_{-6.0}$	0.98
R1 (Centre)	$4.99^{+0.19}_{-0.19}$	$7.23^{+0.13}_{-0.13}$	$55.2^{+1.2}_{-1.2}$	116^{+7}_{-7}	497^{+13}_{-13}	$28.8^{+4.1}_{-4.1}$	0.68
R2	$4.07^{+0.53}_{-0.49}$	$5.58^{+0.34}_{-0.34}$	$9.45^{+0.64}_{-0.64}$	$16.4^{+3.4}_{-3.0}$	$78.1^{+7.5}_{-7.2}$	$4.52^{+0.76}_{-0.76}$	0.32
R3	$6.75^{+0.45}_{-0.42}$	$3.49^{+0.11}_{-0.11}$	$30.1^{+1.9}_{-1.9}$	$18.5^{+3.5}_{-3.1}$	194^{+15}_{-15}	$11.2^{+1.8}_{-1.8}$	0.44
R4	$11.6^{+0.7}_{-0.6}$	$3.21^{+0.10}_{-0.12}$	$53.1^{+4.6}_{-4.6}$	$15.2^{+4.0}_{-3.4}$	328^{+34}_{-33}	$19.0^{+3.3}_{-3.3}$	0.45
R5	$9.41^{+0.63}_{-0.57}$	$3.26^{+0.13}_{-0.12}$	$31.9^{+2.7}_{-2.7}$	$12.3^{+3.2}_{-2.7}$	199^{+21}_{-20}	$11.5^{+2.0}_{-2.0}$	0.49
R2+R3 (South)	$6.96^{+0.34}_{-0.32}$	$3.92^{+0.10}_{-0.10}$	$45.1^{+2.0}_{-2.0}$	$33.4^{+4.5}_{-4.1}$	308^{+18}_{-18}	$17.8^{+2.7}_{-2.7}$	0.57
R4+R5 (North)	$11.2^{+0.5}_{-0.4}$	$3.21^{+0.07}_{-0.08}$	$80.3^{+4.7}_{-4.7}$	$24.2^{+4.2}_{-3.8}$	496^{+35}_{-34}	$28.7^{+4.5}_{-4.5}$	0.61
R2 to R5 (Outer Regions)	$9.12^{+0.27}_{-0.26}$	$3.51^{+0.06}_{-0.06}$	125^{+5}_{-4}	$58.8^{+6.2}_{-5.8}$	809^{+36}_{-36}	$46.8^{+6.9}_{-6.9}$	0.78

[a] see Sect. 2.3

spurs of diffuse X-ray emission on kiloparsec scales which coincide with Hα filaments (Heckman et al. 1995). This emission was interpreted to originate from hot gas which is heated by supernova events with mass-loading from the rims of superbubbles. The observations also led to the speculation that at least part of the hot gas is able to escape the gravitational potential of NGC 1569 (Heckman et al. 1995). These claims were supported by della Ceca et al. (1996) on the basis of ASCA (78 ks) and *ROSAT* PSPC (8 ks) observations. They derive a total X-ray luminosity of $\sim 3 \times 10^{38}$ erg s^{-1} emerging from a soft thermal ($T \simeq 7 \times 10^6$ K) and a hard component. The hard component was attributed to emission from very hot gas ($T \simeq 4 \times 10^7$ K) or alternatively to non-thermal X-ray emission. The limited quality of their data, however, made a complete separation of the point source contribution from the diffuse emission impossible.

Martin, Kobulnicky & Heckman (2002) published a detailed study of NGC 1569 based on the same *Chandra* data as presented here. They find that they require a two temperature model for the hot gas in NGC 1569: a hot component coinciding with the disc ($T \simeq 7 \times 10^6$ K) and a cooler outer component ($T \simeq 3 \times 10^6$ K) adding up to an X-ray luminosity of 8.2×10^{38} erg s^{-1}. According to their analysis, the X-ray emission itself is due to shocks rather than a freely streaming wind. They also claim that the hot wind contains virtually all the metals produced by supernova explosions during the starburst phase which eventually will enrich the intergalactic medium.

4.3.2 Chandra observations revisited

The total X-ray emission of NGC 1569 extends over $\sim 5\farcm0 \times 3\farcm3$ which corresponds to about 3.2×2.1 kpc (see Fig. 3). Twelve point sources were detected (see Sect. 2.2) within the optical and Hα extent. Eight of these sources are located close to the centre of NGC 1569 (P2 to P9; see Fig. 4[a]), three to the east (P10, P11, and P12), and one to the south-west (P1). The extracted count rates of the point sources in the different X-ray bands and the corresponding hardness ratios are listed in Table 10. By far the strongest source is P5, which is located slightly south of the central stellar disc of NGC 1569. An overlay with an *HST*/WFPC2 F555W (corresponding to Johnson V) band image shows that bright stars coincide with the X-ray sources P7 and P9. Source P1 is not in the field of view of the WFPC2 image. Except for P4 and P12, all other objects are located at distances $\lesssim 1''$ to stars and therefore might be related to them. A hardness ratio plot of all X-ray point sources is shown in Fig. 4(b) and 4(c) and their spectra with the fitting models are shown in panel (d) of the same figure. Preliminary thermal plasma emission models provide reasonable fits to the spectra of seven sources (P1, P2, P4, P5, P9, P10, P11, see the corresponding hardness ratio plot) and therefore they are likely SNR candidates or bubbles filled with hot, coronal gas. Four source spectra are well fit by power law models (likely from XRBs; P3, P6, P7, P12) and one spectrum (P8) is a supersoft source for which a black body model is appropriate ($T \simeq 6 \times 10^5$ K). However, only five sources have spectra with a minimum of four counts in at least three spectral bins (P5, P6, P7, P9, P12) – our limit for which we performed final spectral fits. The resulting models and their parameters are listed in Table 11 and displayed in Fig. 4(d). Note that Martin, Kobulnicky & Heckman (2002) detect two more point sources in NGC 1569, based on a somewhat different detection method. They only fitted models to the two brightest sources: P5 and P7. Given the different model fitting parameters and source extraction properties with respect to ours (metallicity, source extraction region, background subtraction) their results for those two point sources are in good agreement with the fits presented here. All X-ray point source luminosities are below the 10^{39} erg s^{-1} threshold for ULXs.

The azimuthally averaged surface brightness ($\mu_{\rm X}$) profiles of the diffuse X-ray emission in all broad bands are well described by exponential declines (see Fig. 3[f] for the total band). As listed in Table 9, the scale lengths of the profiles of all bands are approximately the same: ~ 250 pc. The X-ray distribution, however, is not spherical and in general follows the Hα morphology (Fig. 3[b]). In particular, the prominent Hα arm to the west of NGC 1569 is observed in

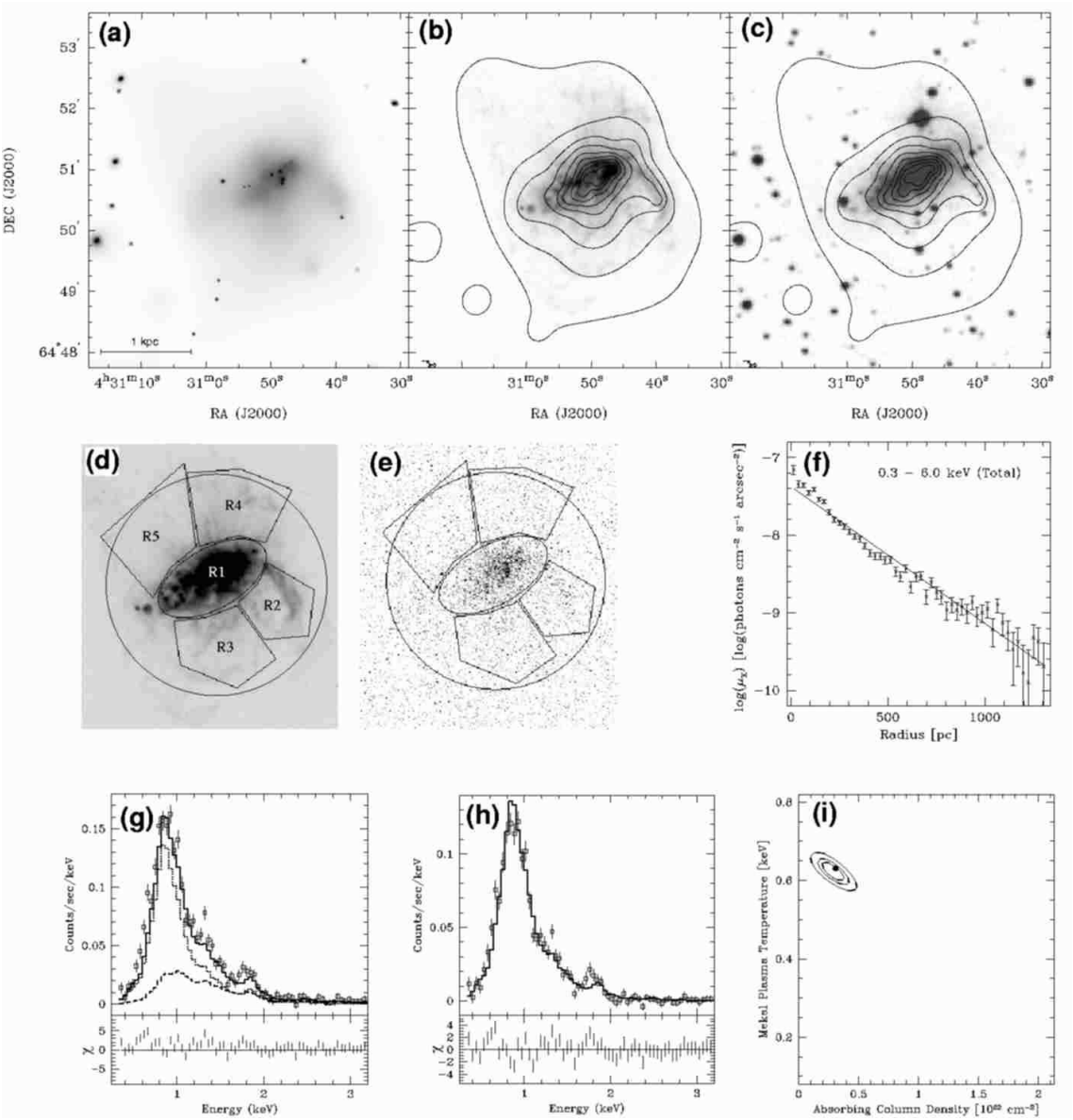

Figure 3. (a) The total, adaptively smoothed X-ray emission of NGC 1569 including point sources on a logarithmic scale. **(b)** Logarithmically scaled Hα image (taken from della Ceca et al. 1996) with contours of the diffuse X-ray emission after the removal of the point sources. Contours of the logarithmic X-ray emission start at and are spaced by $0.1\log(peak flux)$. **(c)** The same contours as in (b) overlaid on an optical DSS image. Images (a), (b), and (c) are on the same scale. **(d)** Definition of the regions used to extract X-ray spectra overlaid on the Hα image. **(e)** The same regions as in (d) but overlaid on the unsmoothed X-ray image including the X-ray point sources. **(f)** Logarithmic, azimuthally averaged surface brightness of the diffuse X-ray emission with the exponential fit overlaid. The centre for this plot is located on the peak of a NIR H-band image. **(g)** The total X-ray spectrum of NGC 1569. Overlaid are the fits for the diffuse emission (*dotted*), the combined point source models (*dashed*), and the point sources plus diffuse emission (*solid*). The lower panels display the normalised residuals $\chi = (data - model)/error$ (note that the error is the uncertainty per energy bin) of the combined model as a function of energy.**(h)** The spectrum of the diffuse X-ray emission as taken from the region displayed as a large circle in panel (e) with the fit result on top. Again, the lower panel shows the error of the fit per bin. **(i)** Confidence regions for the fit of the diffuse X-ray emission [as displayed in (h)] in the $N_H - T$ plane (the normalisation is allowed to vary in the parameter space). The best fit is shown by the *dot* and the confidence levels are 68.3, 90.0, and 99.0 per cent.

broad and narrow optical wavebands as well as in soft X-rays which is slightly offset to the east. The temperature of the hot gas at the centre (region R1, see Fig. 3 and Table 8) of NGC 1569 ($T \simeq 7.2 \times 10^6$ K) is clearly higher than toward the outer regions ($T \simeq 3.5 \times 10^6$ K). The second highest temperature is encountered in the region where the Hα arm is located (R2). Based on the absorbing column density within the regions we can constrain the orientation of the disc of NGC 1569. The hot gas emerging from the southern regions (R2 and R3) is less absorbed than emission coming from the opposite side. Assuming that the outflow is perpendicular to the disc, along the z-axis, this implies that the northern half of the disc of NGC 1569 lies between us and the outflow and hence is the near side, whereas the

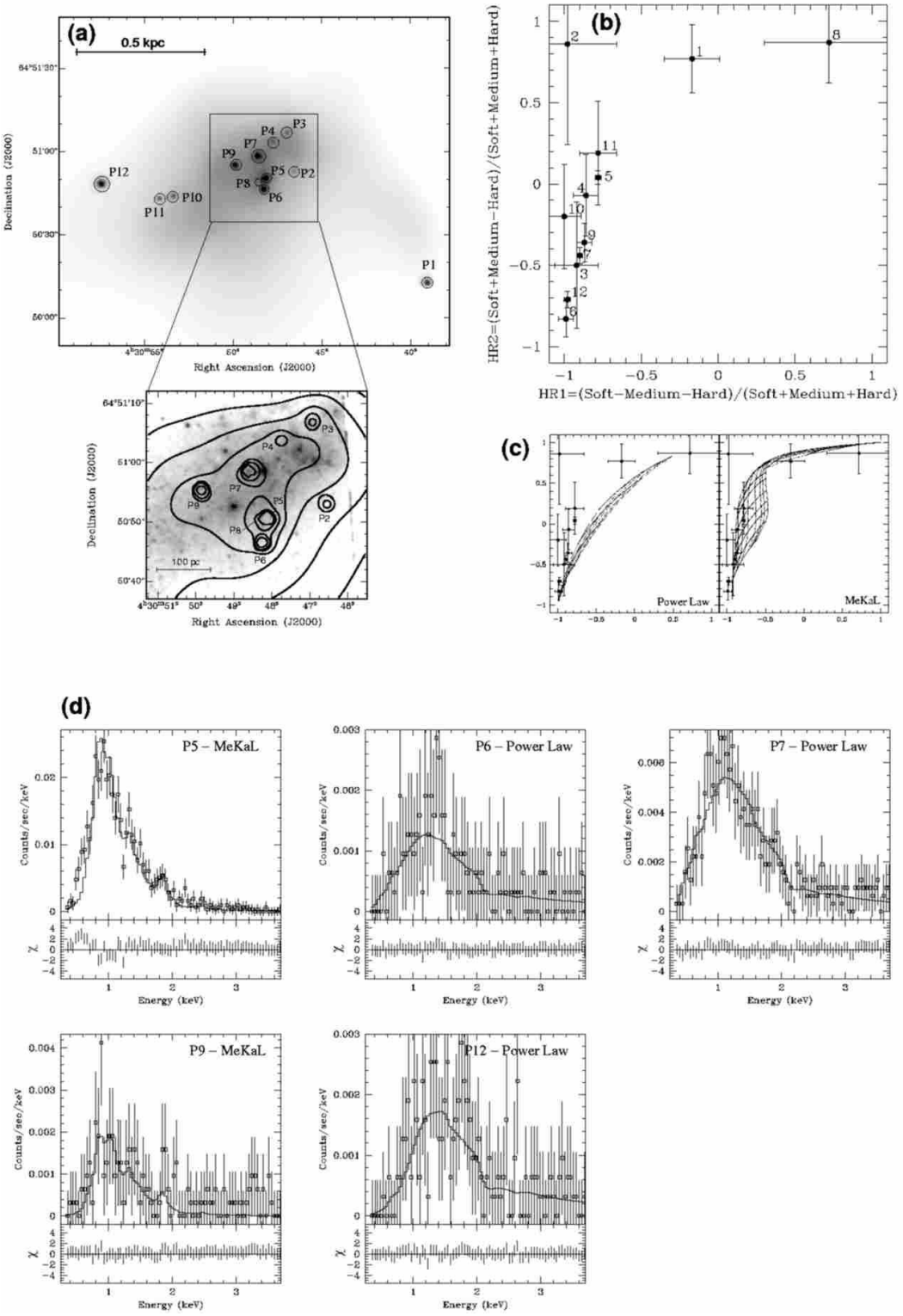

Figure 4. Locations and spectra of the point sources in NGC 1569. **(a)** Numbering scheme of the detected sources overlaid on the adaptively smoothed X-ray image. The blow-up displays an *HST*/WFPC2 F555W (Johnson V) band image of the central region of NGC 1569. Overlaid are contours from the image above. **(b)** A hardness ratio plot of these sources. **(c)** The same sources as plotted in (b) but overlaid on the model grids for a range of power law (*left panel*) and MeKaL thermal plasma (*right panel*; using the H II region metallicity listed in Table 4) models presented in Fig. 2. **(d)** X-ray spectra and the best-fitting models for point sources with counts in at least three spectral bins with four counts minimum per bin. Normalised residuals $\chi = (data - model)/error$ (the error is the uncertainty per energy bin) are plotted below the spectra. For the model selection see Sect. 4 and for the count rates, hardness ratios and fitting parameters Tables 10 and 11).

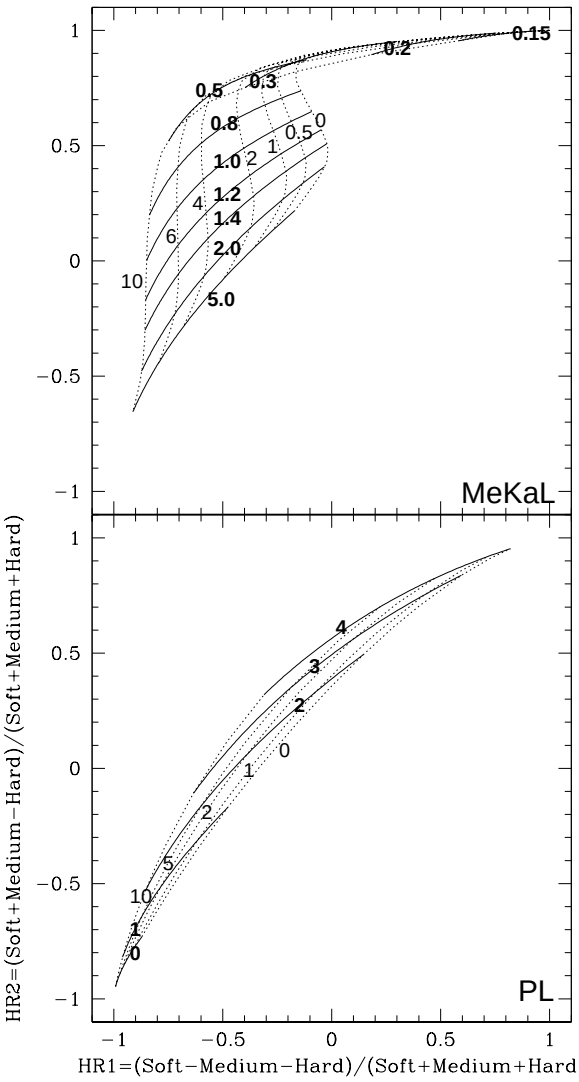

Figure 2. Hardness ratio plots of MeKaL thermal plasma (**top**) and PL (**bottom**) models. Whereas the PL models are more or less distributed along a diagonal strip extending from the lower left to the upper right, the MeKaL models occupy a region in the upper left corner. *Dotted lines* mark models at constant absorbing column densities $N_{\rm H}$ (*normal fonts*, given in units of 10^{21} cm^{-2}). Models at a constant Temperature T (MeKaL) or power law index Γ (PL) are displayed as *solid lines*) and are labelled with *bold fonts*. Temperatures in the MeKaL model are given in units of keV (1 keV corresponds to 1.1604×10^7 K). The grids presented in this figure are repeated at a smaller scale in panels (c) of Figs. 4, 6, 8, 10, 12, and 14 with overplotted the location of the point sources in these hardness ratio plots.

southern part of the disc points away (in agreement with Martin, Kobulnicky & Heckman 2002). The MeKaL fit to the spectrum of the total diffuse X-ray emission results in an unabsorbed luminosity of 4.2×10^{38} erg s^{-1}. Adding up the MeKaL X-ray luminosity of the hot gas and the luminosities of the point sources with reliable fits (Tables 8 and 11) we derive a total X-ray luminosity of 8.3×10^{38} erg s^{-1} (see also the total spectrum in Fig. 3). This value is ~ 3 times larger than the *ROSAT* results but lower than the X-ray luminosity obtained by *EINSTEIN* (note that *ROSAT* and *EINSTEIN* were not able to provide sufficient angular resolution for an independent treatment of the individual point sources and the diffuse emission). The mean temperature of the hot gas ($\sim 7\times10^6$ K) of the *Chandra* observations as well as the central and outer regions temperatures are in good agreement with those derived by previous observations (see della Ceca et al. 1996; Martin, Kobulnicky & Heckman 2002).

Table 9. Results of fits of exponential functions to the azimuthally averaged X-ray surface brightness profiles in the different bands (h: exponential scale length in pc).

	$h_{\rm Total}$	$h_{\rm Soft}$	$h_{\rm Medium}$	$h_{\rm Hard}$
NGC 1569	208 ± 6	229 ± 14	211 ± 6	212 ± 15
NGC 3077	186 ± 10	296 ± 49	200 ± 8	135 ± 21
NGC 4214	145 ± 12	127 ± 19	148 ± 21	187 ± 60
NGC 4449	579 ± 15	590 ± 22	505 ± 15	623 ± 68
NGC 5253	109 ± 9	124 ± 13	101 ± 8	60 ± 6
He 2-10	186 ± 15	273 ± 37	166 ± 11	125 ± 9

4.4 NGC 3077 (UGC 5398)

4.4.1 Previous X-ray observations and results

The first X-ray observations of NGC 3077 were performed by the *EINSTEIN* satellite and resulted in an upper limit for its X-ray luminosity of $< 4\times10^{38}$ erg s^{-1} (Fabbiano, Kim & Trinchieri 1992). *ROSAT* PSPC data (7 ks) were analysed by Bi, Arp & Zimmermann (1994). They found evidence for extended X-ray emission in NGC 3077. A fit of an RS thermal plasma model to their X-ray spectrum revealed a temperature of $\sim 7\times10^6$ K and a luminosity of 2×10^{38} erg s^{-1}. Ott, Martin & Walter (2003) published a paper on the same *Chandra* data that are presented here. Their main results are that individual, prominent Hα shells appear to be filled with X-ray emitting, hot thermal plasma (temperatures ranging from ~ 1 to 5×10^6 K). The plasma stored in the shells has pressures of $\sim 10^{5-6}$ K cm^{-3} which is most likely what drives their expansion. The total X-ray luminosity was determined to be in the range of $2-5\times10^{39}$ erg s^{-1} depending on the plasma model used. About 85 per cent of this emission can be attributed to the diffuse, hot thermal plasma and the remainder is emitted by six point sources (two XRBs, three SNR candidates, and a supersoft source).

4.4.2 Chandra observations revisited

The diffuse X-ray emission of NGC 3077 has an extent of $\sim 1'$ which corresponds to about 1 kpc (see (Fig. 5[a]). Six point sources are detected within the optical and Hα extent of NGC 3077 (Fig. 6): Three sources (P2, P3, and P4) are well modeled by thermal plasmas and are likely young supernova remnants or small bubbles filled with hot gas. Two (P5 and P6) show power law spectra and one (P1) is a supersoft source in the outskirts of NGC 3077. Only P1, P4, and P6, however, exceed our threshold for spectral fitting (see Tables 13 and 14 for the point source properties). A comparison with optical *HST*/WFPC2 data (Fig. 6[a]) shows that a bright star is located just between the two X-ray sources P5 and P6. Given the absolute positional uncertainties of

Table 10. Positions, count rates and hardness ratios of the point sources in NGC 1569. The Right Ascension and Declination are given in ^{h} ^{m} ^{s} and $^\circ$ $'$ $''$ (J2000), respectively. The count rates of the total, soft, medium, and hard bands are in units of 10^{-5} cts s^{-1}. See Fig. 4 for the locations of the point sources coinciding with this galaxy as well as for their distribution in a hardness ratio plot.

No.	RA	DEC	Total	Soft	Medium	Hard	HR1	HR2
P1	04 30 39.0	+64 50 12.8	50.40 ± 9.59	20.86 ± 5.39	23.87 ± 6.91	5.66 ± 3.89	-0.17 ± 0.18	$+0.77 \pm 0.21$
P2	04 30 46.5	+64 50 52.3	24.28 ± 8.81	0.21 ± 3.86	22.41 ± 6.49	1.65 ± 4.53	-0.98 ± 0.32	$+0.86 \pm 0.62$
P3	04 30 46.9	+64 51 06.9	33.38 ± 10.22	1.39 ± 2.41	6.95 ± 6.37	25.03 ± 7.62	-0.92 ± 0.14	-0.50 ± 0.39
P4	04 30 47.8	+64 51 03.7	59.54 ± 10.90	4.17 ± 2.41	23.47 ± 7.52	31.90 ± 7.51	-0.86 ± 0.08	-0.07 ± 0.25
P5	04 30 48.1	+64 50 50.8	1809 ± 52	197 ± 17	742 ± 34	870 ± 35	-0.78 ± 0.02	$+0.04 \pm 0.04$
P6	04 30 48.3	+64 50 46.3	192.5 ± 20.4	1.27 ± 5.05	14.90 ± 9.79	176.4 ± 17.2	-0.99 ± 0.05	-0.83 ± 0.11
P7	04 30 48.6	+64 50 58.3	784 ± 35	37.55 ± 8.91	183.6 ± 18.2	563 ± 29	-0.90 ± 0.02	-0.44 ± 0.05
P8	04 30 48.6	+64 50 49.4	26.24 ± 9.05	22.53 ± 6.47	2.04 ± 5.22	1.67 ± 3.58	$+0.72 \pm 0.42$	$+0.87 \pm 0.25$
P9	04 30 49.9	+64 50 55.2	193.4 ± 19.3	12.46 ± 4.63	49.32 ± 11.22	131.6 ± 15.0	-0.87 ± 0.05	-0.36 ± 0.12
P10	04 30 53.4	+64 50 44.3	34.77 ± 7.99	0.00 ± 1.97	13.91 ± 5.20	20.86 ± 5.73	-1.00 ± 0.11	-0.20 ± 0.32
P11	04 30 54.2	+64 50 43.0	37.66 ± 8.44	4.17 ± 2.41	18.17 ± 6.35	15.32 ± 5.01	-0.78 ± 0.12	$+0.19 \pm 0.32$
P12	04 30 57.4	+64 50 48.6	312.9 ± 21.1	2.78 ± 2.78	43.11 ± 7.99	267.0 ± 19.4	-0.98 ± 0.02	-0.71 ± 0.05

Table 11. Parameters of the fitted models to the point sources in NGC 1569 (N_H: absorbing column density, T/γ: temperature (MeKaL [MEK], black body [BB]) or power law photon index (PL, $I \propto E^{-\gamma}$), $Norm/Ampl^a$: Normalisation (MEK) or Amplitude (PL, BB), $F_{\rm X}^{\rm abs}$: absorbed flux ($0.3 - 8.0$ keV), $F_{\rm X}$: unabsorbed flux, $L_{\rm X}$: unabsorbed luminosity). Sources which do not provide sufficient counts (at least three spectral bins with four counts minimum) are not listed. See Fig. 4(d) for the individual spectra and fits. The last column displays the CXOU numbering of the sources in Martin, Kobulnicky & Heckman (2002). Errors in the fitted parameters are conservatively estimated to be of order 30 per cent.

No.	Model	N_H	T/γ	$Norm/Ampl^a$	$F_{\rm X}^{\rm abs}$	$F_{\rm X}$	$L_{\rm X}$	
		[10^{21} cm^{-2}]	[10^6 K/–]	[10^{-5}]	[10^{-15} erg s^{-1} cm^{-2}]		[10^{37} erg s^{-1}]	CXOU
P5	MEK	13.5	6.88	44.5	55.03	397.8	23.03	043048.1+645050
P6	PL	8.54	2.02	0.57	19.16	35.13	2.03	043048.2+645046
P7	PL	8.82	2.49	2.69	52.03	153.4	8.88	043048.6+645058
P9	MEK	17.52	6.51	5.64	4.87	49.93	2.89	043049.8+645055
P12	PL	17.64	2.33	1.31	25.78	74.56	4.32	043057.4+645048

[a] see Sect. 2.3

the *HST* and *Chandra* observations, this could be the donor star in the XRB scenario for one of the sources. P5 and P6, however, are only $\sim 1''$ apart and it is therefore not possible to clearly attribute P5 or P6 to this optical counterpart. Ott, Martin & Walter (2003) argue that P5 might also be a background AGN given the high absorbing column density along this line of sight. Close to the centre of NGC 3077 an absorption feature stretches toward the south-west and the point of strongest absorption coincides with the X-ray point source P4. No obvious optical features can be detected at the positions of P1, P2, and P3. A more detailed analysis of the X-ray point sources is given in Ott, Martin & Walter (2003).

The morphology of the diffuse X-ray emission of NGC 3077 is similar to its Hα distribution on a global scale (Fig. 5[b]). Viewed on smaller scales, however, it turns out that Hα filaments surround certain areas of diffuse X-ray emission and we can attribute this morphology to expanding superbubbles filled with hot coronal gas (for a characterisation of the individual superbubbles, see Ott, Martin & Walter 2003). An exponential function provides a good fit to the azimuthally averaged surface brightness profiles of the diffuse X-ray emission (Fig. 5[f]). From Table 9 we derive that the soft emission (scale length $h_{\rm Soft} \simeq 300$ pc) is about twice as extended as compared to the hard emission ($h_{\rm Hard} \simeq 140$ pc). Hardening of the X-ray emission due to photoelectric absorption can be made responsible for at least part of this effect (see the prominent optical absorption features in Fig. 6[a]). The fits of thermal plasma models to spectra which were obtained from individual regions (Figs. 5[d] and [e]) show some temperature gradient from the centre toward the outer regions (Table 12). The orientation of NGC 3077 as traced by photoelectric absorption cannot be constrained based on our analysis. The total, diffuse X-ray luminosity is 1.7×10^{39} erg s^{-1}; adding the point source luminosities result in 1.9×10^{39} erg s^{-1}. The X-ray luminosities as derived from *ROSAT* and *EINSTEIN* data are one order of magnitude lower (Bi, Arp & Zimmermann 1994); the likely reason for this discrepancy is an approximately seven times lower absorbing column density used in their fits. In addition, Bi, Arp & Zimmermann (1994) use a bremsstrahlung spectrum rather than a thermal plasma model and were not able to subtract the X-ray point sources.

4.5 NGC 4214 (NGC 4228, UGC 7278)

4.5.1 Previous X-ray observations and results

EINSTEIN was the first X-ray telescope to observe NGC 4214 and Fabbiano, Kim & Trinchieri (1992) derived an upper limit to the X-ray luminosity of 1.5×10^{40} erg s^{-1}. *ROSAT* observations were performed with the HRI instrument for $\sim$ 43 ks (Roberts & Warwick 2000) as part of a large survey. They detected a point-like nuclear source with an X-ray luminosity of 1.8×10^{38} erg s^{-1}. Recently, Hartwell et al. (2004) published a more detailed analysis of

Table 12. Results of MeKaL collisional thermal plasma model fits applied to the X-ray spectra of different regions in NGC 3077 (see panels [d] and [e] in Fig. 5 for the definition of the regions).

Region	$N_{\rm H}$	T	$Norm^a$	$F_{\rm X}^{\rm abs}$	$F_{\rm X}$	$L_{\rm X}$	χ^2_{red}
	$[10^{21}\,{\rm cm}^{-2}]$	$[10^6\,{\rm K}]$	$[10^{-5}]$	$[10^{-15}\,{\rm erg\,s^{-1}\,cm^{-2}}]$	$[10^{-15}\,{\rm erg\,s^{-1}\,cm^{-2}}]$	$[10^{37}\,{\rm erg\,s^{-1}}]$	
Total	$4.71^{+0.11}_{-0.11}$	$2.32^{+0.04}_{-0.04}$	$50.7^{+2.8}_{-2.8}$	$33.6^{+5.6}_{-5.1}$	1062^{+71}_{-69}	165^{+26}_{-26}	0.43
R1 (Centre)	$0.86^{+0.32}_{-0.28}$	$6.04^{+0.72}_{-0.87}$	$0.39^{+0.05}_{-0.05}$	$6.16^{+1.95}_{-1.85}$	$11.2^{+1.6}_{-1.8}$	$1.74^{+0.37}_{-0.37}$	0.11
R2	$4.36^{+0.17}_{-0.15}$	$2.18^{+0.04}_{-0.04}$	$20.9^{+1.8}_{-1.8}$	$13.0^{+3.4}_{-3.0}$	420^{+42}_{-41}	$65.1^{+11.3}_{-11.3}$	0.24
R3	$3.20^{+0.29}_{-0.25}$	$3.21^{+0.20}_{-0.19}$	$2.23^{+0.28}_{-0.29}$	$6.76^{+2.63}_{-2.16}$	$52.1^{+7.7}_{-7.3}$	$8.08^{+1.66}_{-1.66}$	0.17
R4	$6.14^{+0.57}_{-0.40}$	$1.60^{+0.05}_{-0.11}$	$43.0^{+11.9}_{-11.9}$	$2.44^{+2.42}_{-1.49}$	644^{+208}_{-224}	$99.8^{+37.5}_{-37.5}$	0.18
R2 to R4 (Outer Regions)	$4.52^{+0.14}_{-0.13}$	$2.30^{+0.04}_{-0.04}$	$30.5^{+2.2}_{-2.2}$	$21.6^{+4.7}_{-4.1}$	637^{+54}_{-53}	$98.7^{+16.3}_{-16.3}$	0.44

[a] see Sect. 2.3

Table 13. Positions, count rates and hardness ratios of the point sources in NGC 3077. The Right Ascension and Declination are given in $^h\ ^m\ ^s$ and $^\circ\ '\ ''$ (J2000), respectively. The count rates of the total, soft, medium, and hard emission are in units of $10^{-5}\,{\rm cts\,s^{-1}}$. See Fig. 6 for the locations of the point sources coinciding with this galaxy as well as for their distribution in a hardness ratio plot.

No.	RA	DEC	Total	Soft	Medium	Hard	HR1	HR2
P1	10 03 17.8	+68 44 16.0	78.60 ± 12.97	74.86 ± 12.69	1.87 ± 1.87	1.87 ± 1.87	$+0.90 \pm 0.07$	$+0.95 \pm 0.05$
P2	10 03 17.9	+68 43 57.3	31.81 ± 10.75	3.74 ± 5.92	18.71 ± 7.48	9.35 ± 4.95	-0.76 ± 0.33	$+0.41 \pm 0.53$
P3	10 03 18.3	+68 44 03.8	50.53 ± 9.72	5.61 ± 3.24	35.56 ± 8.15	9.36 ± 4.18	-0.78 ± 0.12	$+0.63 \pm 0.31$
P4	10 03 18.8	+68 43 56.4	248.9 ± 21.7	3.74 ± 3.74	87.96 ± 12.83	157.2 ± 17.2	-0.97 ± 0.03	-0.26 ± 0.11
P5	10 03 19.1	+68 44 01.4	213.3 ± 21.0	0.00 ± 0.00	3.74 ± 4.58	209.6 ± 20.5	-1.00 ± 0.00	-0.96 ± 0.04
P6	10 03 19.1	+68 44 02.3	222.7 ± 21.1	5.61 ± 3.24	28.07 ± 8.16	189.0 ± 19.2	-0.95 ± 0.02	-0.70 ± 0.08

the same Chandra data as discussed here. They fitted a two-temperature thermal plasma with $T = 1.6$ and 6.0×10^6 K to the diffuse X-ray emission.

4.5.2 Chandra observations revisited

The extent of the diffuse X-ray emission centred on NGC 4214 is about 1.′3 (corresponding to 1 kpc) and slightly elongated along the north-south axis (see Fig. 7[a]). A second, smaller X-ray emitting region is found close to an H II region at the northern tip of this galaxy (Fig. 7[a] and [b]), which, however, is not significant and might be an artefact from the adaptive smoothing process (note that this feature cannot be seen when smoothed with a Gaussian kernel of fixed size). The X-ray emitting region is much smaller than the Hα distribution ($6.'8 \times 3.'2$).

Four point sources are detected coinciding with the diffuse X-ray and Hα emission of NGC 4214. A comparison with *HST*/WFPC2 F555W data shows that P2 and P4 coincide with the location of bright stars. No optical counterpart can be found for P3 (with a count rate of $1.2 \times 10^{-2}\,{\rm cts\,s^{-1}}$ it is by far the strongest source) and P1 is not in the WFPC2 field of view (see Fig. 8). All point sources, however, are located on or close to H II regions. In particular, P2 and P3 are near the centre of NGC 4214 where the current star formation rate is highest. The positions, count rates and hardness ratios of the point sources are listed in Table 16. For P3 and P4, where enough counts were accumulated, the models which provided the best fits are a thermal plasma and a power law, respectively (see Fig. 8[b], [c], and [d]). Their parameters are listed in Table 17. The strongest source, P3, is most likely identical to the source observed by *ROSAT* and its luminosity is with $2.6 \times 10^{38}\,{\rm erg\ s^{-1}}$ in good agreement with the *ROSAT* measurements.

The azimuthally averaged, diffuse X-ray emission is well fit by an exponential law with similar scale lengths in all bands (~ 145 pc, see Table 9 and Fig. 7[f]) but shows the X-ray surface brightness flattening off toward the centre and a local maximum at large radii. The temperature of the hot gas ($T \simeq 2.2 \times 10^6$ K – somewhat higher as compared to the low temperature component fitted by Hartwell et al. 2004) does not show any variation over the field of view. The northern portion of the diffuse X-ray emission, however, is about an order of magnitude more absorbed than the south (see Table 15). Therefore, the north of the disc of NGC 4214 is directed toward the observer and shadows the X-ray emitting superwind whereas the southern part of the disc points away and is situated behind the hot gas. The total X-ray luminosity of the diffuse component is determined to $7.7 \times 10^{39}\,{\rm erg\ s^{-1}}$ (see also Fig. 7(h); note that the errors of the fits are quite large as can be seen by the size of the confidence regions in Fig. 7[i]). The total X-ray emission (luminosity: $8.5 \times 10^{39}\,{\rm erg\ s^{-1}}$; point sources plus MeKaL diffuse emission) is shown in Fig. 7(g) and is dominated by the flux of the point sources, in contrast to the other galaxies in our sample.

4.6 NGC 4449 (UGC 7592)

4.6.1 Previous X-ray observations and results

Blair, Kirshner & Winkler (1983) were the first to report an *EINSTEIN* X-ray detection of NGC 4449. They concen-

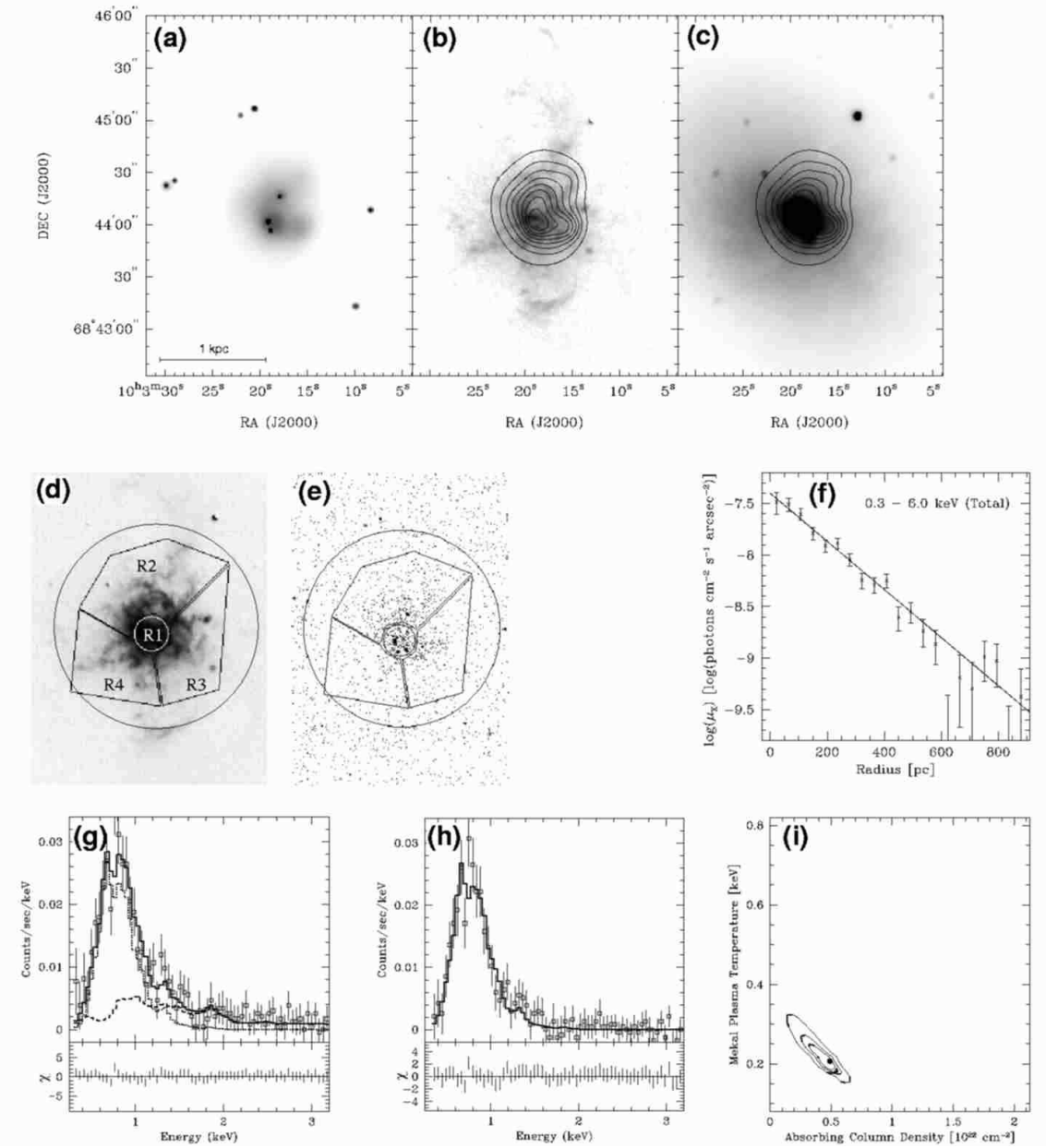

Figure 5. Images and spectra of the X-ray emission of NGC 3077. See the caption of Fig. 3 for details. The contours of the logarithmic X-ray emission in panels (b) and (c) are spaced by $0.1\log(peakflux)$ and start at $0.2\log(peakflux)$ (continuum subtracted Hα image taken from Martin 1997, and optical Calar Alto 2.2m *R*–band image from Walter et al. 2002).

Table 14. Parameters of the fitted X-ray emission models to the point sources in NGC 3077. See the caption of Table 11 for details and Fig. 6(d) for the individual spectra and fits. Note that contrary to the tables in Ott, Martin & Walter (2003) the absorbing column densities listed here represent internal absorption of NGC 3077 only. The last column lists the corresponding source notation in Ott, Martin & Walter (2003).

No.	Model	N_H	T/γ	$Norm/Ampl^a$	F_X^{abs}	F_X	L_X	
		$[10^{21}$ cm$^{-2}]$	$[10^6$ K/–]	$[10^{-5}]$	$[10^{-15}$ erg s^{-1} cm$^{-2}]$		$[10^{37}$ erg s$^{-1}]$	Cross Ident.
P1	BB	0.0	0.94	2022	2.88	5.92	0.92	S4
P4	MEK	8.77	9.27	3.28	10.44	85.75	13.30	S1
P6	PL	2.93	1.00	3.77	58.05	65.14	10.10	S3

[a] see Sect. 2.3

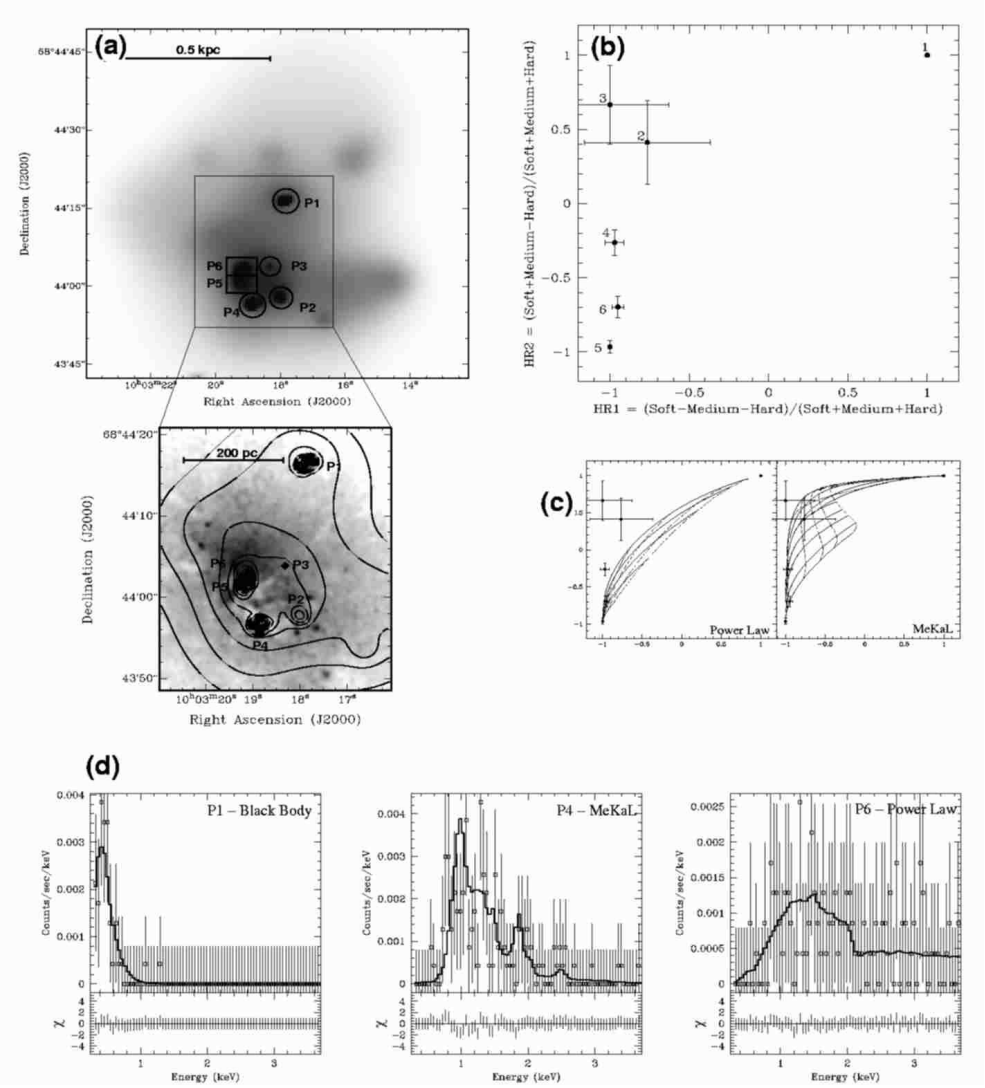

Figure 6. Locations and spectra of the point sources in NGC 3077. See caption of Fig. 4 for details. The *HST*/WPFC2 image shown in the blow-up of panel (a) was obtained in the F814W filter. The count rates, hardness ratios and model parameters are listed in Tables 13 and 14.

Table 15. Results of MeKaL collisional thermal plasma model fits applied to the X-ray spectra of different regions in NGC 4214 (see panels [d] and [e] in Fig. 7 for the definition of the regions).

Region	$N_{\rm H}$	T	$Norm^a$	$F_{\rm X}^{\rm abs}$	$F_{\rm X}$	$L_{\rm X}$	χ^2_{red}
	$[10^{21}\,{\rm cm}^{-2}]$	$[10^6\,{\rm K}]$	$[10^{-5}]$	$[10^{-15}\,{\rm erg\,s^{-1}\,cm^{-2}}]$	$[10^{-15}\,{\rm erg\,s^{-1}\,cm^{-2}}]$	$[10^{37}\,{\rm erg\,s^{-1}}]$	
Total	$9.87^{+0.59}_{-0.52}$	$2.17^{+0.06}_{-0.06}$	129^{+14}_{-14}	$37.9^{+12.9}_{-10.6}$	759^{+98}_{-95}	$75.9^{+14.5}_{-14.5}$	0.14
R1 (Centre)	$10.1^{+1.4}_{-1.1}$	$2.80^{+0.27}_{-0.28}$	$22.7^{+5.3}_{-5.3}$	$12.5^{+9.8}_{-6.7}$	155^{+44}_{-41}	$15.5^{+4.9}_{-4.9}$	0.04
R2 (North)	$14.4^{+1.2}_{-0.9}$	$1.64^{+0.07}_{-0.08}$	300^{+71}_{-71}	$11.7^{+10.0}_{-6.5}$	1321^{+397}_{-377}	132^{+44}_{-44}	0.10
R3 (South)	$2.99^{+1.13}_{-0.85}$	$2.60^{+0.33}_{-0.33}$	$6.11^{+1.45}_{-1.45}$	$12.2^{+9.2}_{-6.7}$	$40.8^{+12.1}_{-12.5}$	$4.08^{+1.38}_{-1.38}$	0.07
R2+R3 (Outer Regions)	$2.91^{+0.67}_{-0.56}$	$2.68^{+0.21}_{-0.24}$	$12.2^{+1.8}_{-1.8}$	$25.8^{+11.3}_{-9.6}$	$82.3^{+14.9}_{-15.6}$	$8.23^{+1.95}_{-1.95}$	0.14

[a] see Sect. 2.3

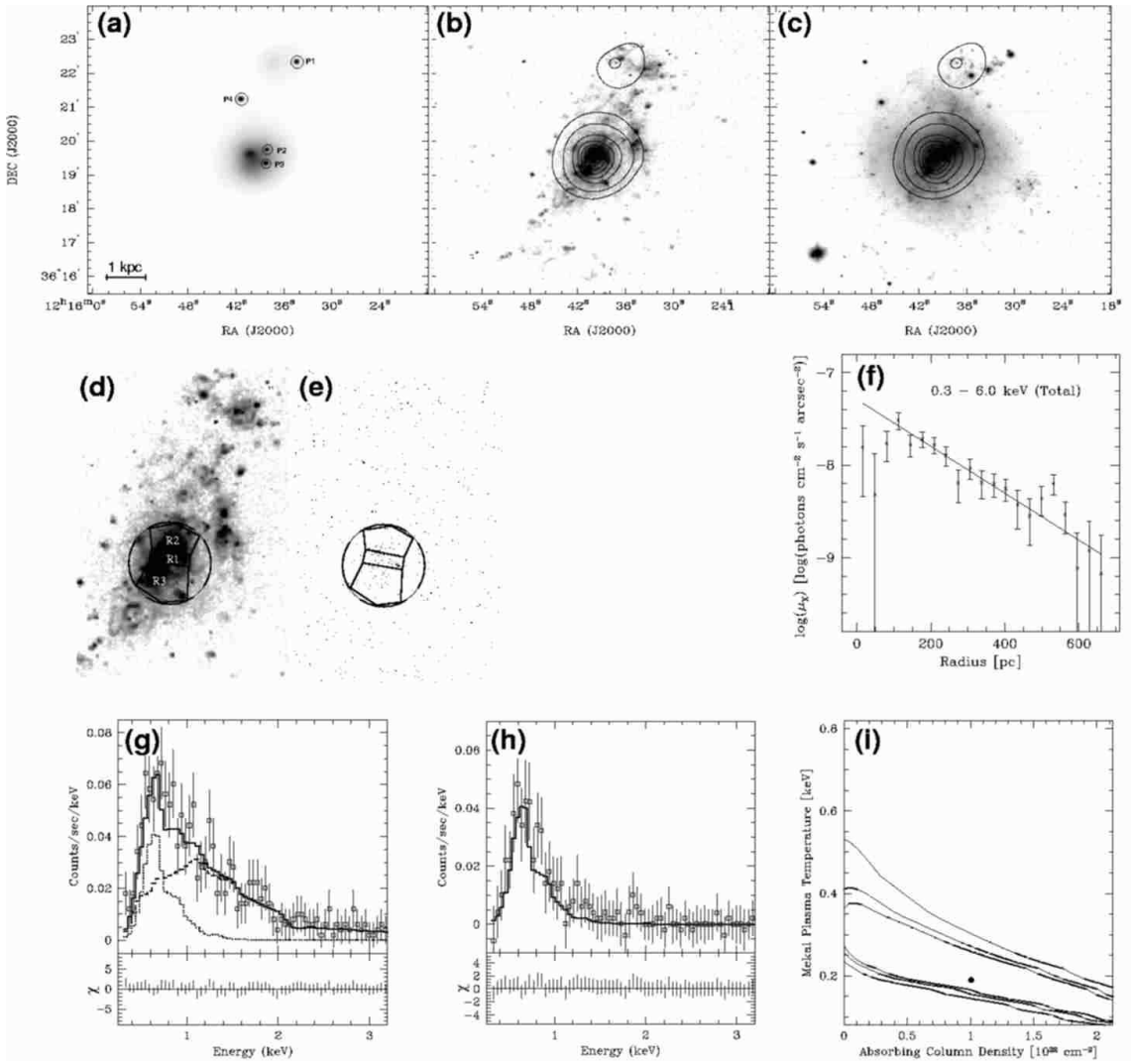

Figure 7. Images and spectra for the X-ray emission of NGC 4214. See the caption of Fig. 3 for details. The outermost contour of the logarithmic X-ray emission displays the $0.15\log(peakflux)$. The other contours are spaced by $0.1\log(peakflux)$ starting at a $0.2\log(peakflux)$ level (B–band and continuum subtracted Hα images taken from Walter et al. 2001).

Table 16. Positions, count rates and hardness ratios of the point sources in NGC 4214. The Right Ascension and Declination are given in ^{h} ^{m} ^{s} and $^\circ$ $'$ $''$ (J2000), respectively. The count rates of the total, soft, medium, and hard emission are in units of 10^{-5} cts s^{-1}. See Fig. 8 for the locations of the point sources coinciding with this galaxy as well as for their distribution in a hardness ratio plot.

No.	RA	DEC	Total	Soft	Medium	Hard	HR1	HR2
P1	12 15 34.4	+36 22 20.5	140.9 ± 39.4	8.81 ± 8.81	52.8 ± 21.6	79.3 ± 31.8	-0.88 ± 0.12	-0.13 ± 0.31
P2	12 15 38.2	+36 19 45.1	405.1 ± 64.7	70.5 ± 30.5	79.3 ± 31.8	255.4 ± 47.4	-0.65 ± 0.13	-0.26 ± 0.18
P3	12 15 38.2	+36 19 21.4	3162 ± 171	255.4 ± 55.0	854.3 ± 87.6	2052 ± 137	-0.84 ± 0.03	-0.30 ± 0.06
P4	12 15 41.4	+36 21 14.9	951.2 ± 91.5	140.9 ± 35.2	140.9 ± 35.2	669.3 ± 76.8	-0.70 ± 0.07	-0.41 ± 0.09

Table 17. Parameters of the fitted X-ray emission models to the point sources in NGC 4214. See the caption of Table 11 for details and Fig. 8(d) for the individual spectra and fits. The last column lists the source number allocated by Hartwell et al. (2004).

No.	Model	N_H [10^{21} cm^{-2}]	T/γ [10^6 K/–]	$Norm/Ampl^a$ [10^{-5}]	$F_{\rm X}^{\rm abs}$ [10^{-15} erg s^{-1} cm^{-2}]	$F_{\rm X}$	$L_{\rm X}$ [10^{37} erg s^{-1}]	Cross Ident.
P3	MEK	4.36	39.4	18.82	186	262	26.36	10
P4	PL	5.87	1.93	1.39	157.62	89.70	9.03	15

[a] see Sect. 2.3

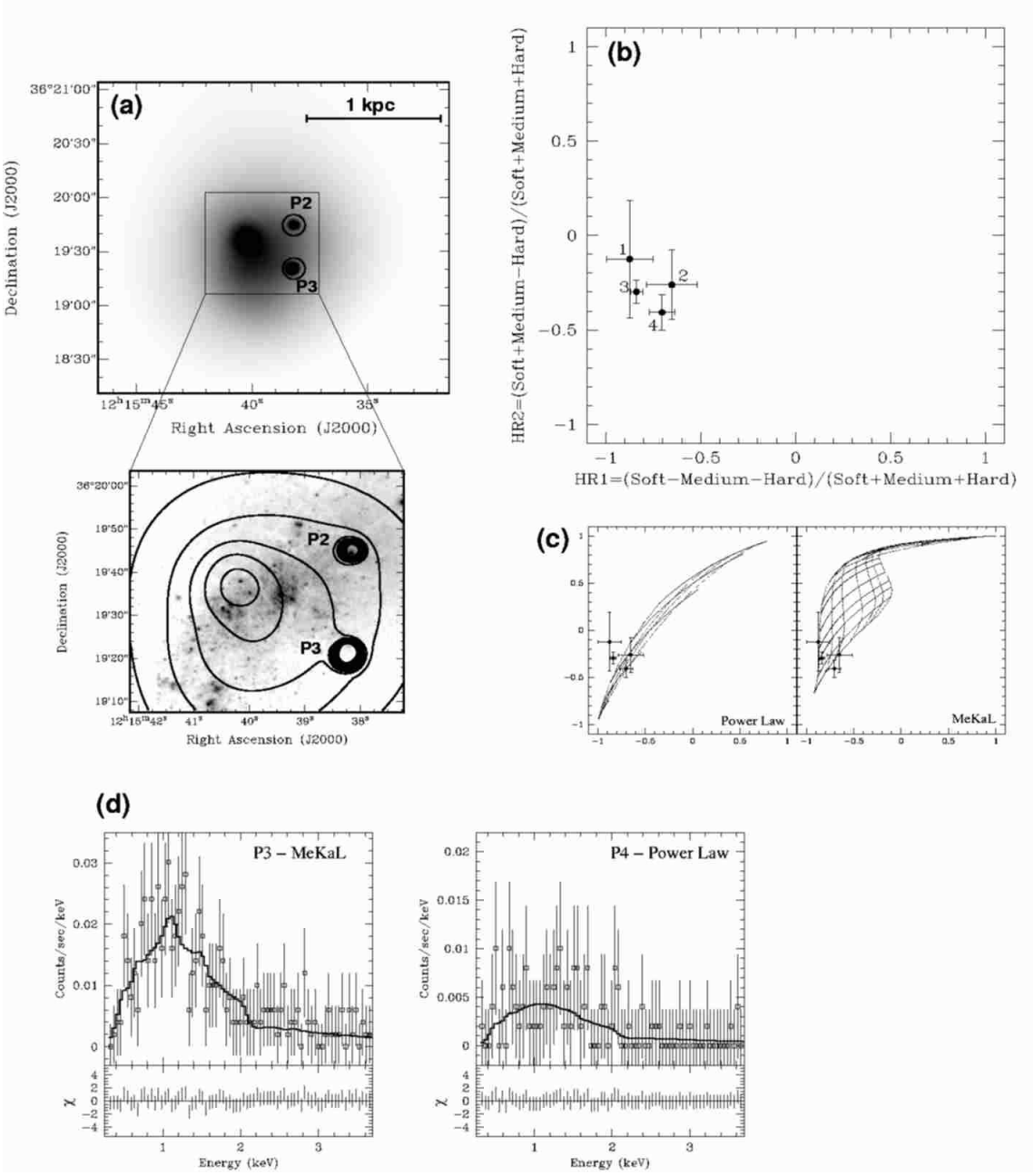

Figure 8. Locations and spectra of the point sources in NGC 4214. See caption of Fig. 4 for details. The count rates, hardness ratios and fitted parameters are listed in Tables 16 and 17.

trated their study on a strong point source (P9, see below) which, based on radio continuum measurements, was previously classified as a SNR (Bignell & Seaquist 1983). They derived an extraordinary high X-ray luminosity of $\sim 10^{39}$ erg s^{-1}. Based on *ROSAT* HRI (15 ks) and PSPC (8 ks) data, Vogler & Pietsch (1997) detected seven point sources embedded in diffuse X-ray emission (combined X-ray luminosity of 2.5×10^{39} erg s^{-1}). They attributed the diffuse emission to hot thermal gas ($T \simeq 3 \times 10^6$ K) and concluded that the global X-ray emission resembles that of the Large Magellanic Cloud after scaling for the different galaxy masses. Bomans, Chu & Hopp (1997) assigned the diffuse thermal emission to active star forming regions, to outflows, and to the interior of a supergiant shell which was detected via Hα observations (PSPC data: 2 ks, HRI data: 32 ks). della Ceca, Griffiths & Heckman (1997) combined the *ROSAT* PSPC data with observations from ASCA (45 ks). In addition to the hard emission from the point source population they postulate a soft ($T \simeq 8 \times 10^6$ K) and a very soft ($T \simeq 3 \times 10^6$ K) diffuse thermal X-ray component. They concluded that mass-loading plays an important role in NGC 4449. In addition, they inferred that the gas is hot enough the be blown-out, i.e., to leave the gravitational potential of NGC 4449. More recently, Summers et al. (2003) published a detailed analysis of the *Chandra* data also presented here. They fit a two-temperature thermal plasma

Table 18. Results of MeKaL collisional thermal plasma model fits applied to the X-ray spectra of different regions in NGC 4449 (see panels [d] and [e] in Fig. 9 for the definition of the regions).

Region	$N_{\rm H}$	T	$Norm^a$	$F_{\rm X}^{\rm abs}$	$F_{\rm X}$	$L_{\rm X}$	χ^2_{red}
	$[10^{21}\,{\rm cm}^{-2}]$	$[10^6\,{\rm K}]$	$[10^{-5}]$	$[10^{-15}\,{\rm erg\,s^{-1}\,cm^{-2}}]$	$[10^{-15}\,{\rm erg\,s^{-1}\,cm^{-2}}]$	$[10^{37}\,{\rm erg\,s^{-1}}]$	
Total	$7.19^{+0.10}_{-0.10}$	$2.98^{+0.03}_{-0.03}$	353^{+7}_{-7}	393^{+21}_{-20}	2481^{+55}_{-55}	452^{+65}_{-65}	1.07
R1 (Centre)	$7.87^{+0.23}_{-0.22}$	$3.12^{+0.07}_{-0.07}$	71^{+3}_{-3}	$75.9^{+9.2}_{-8.5}$	510^{+26}_{-26}	$92.8^{+14.0}_{-14.0}$	0.26
R2	$1.08^{+0.25}_{-0.23}$	$4.43^{+0.23}_{-0.22}$	$9.93^{+0.51}_{-0.51}$	$56.8^{+8.7}_{-7.9}$	$84.1^{+6.8}_{-6.5}$	$15.3^{+2.5}_{-2.5}$	0.23
R3	$9.66^{+0.25}_{-0.24}$	$2.91^{+0.06}_{-0.06}$	$99.7^{+4.6}_{-4.6}$	$68.5^{+9.1}_{-8.5}$	694^{+38}_{-37}	126^{+19}_{-19}	0.40
R4	$7.89^{+0.32}_{-0.30}$	$2.68^{+0.07}_{-0.07}$	$46.7^{+3.0}_{-3.0}$	$37.7^{+7.0}_{-6.3}$	315^{+24}_{-23}	$57.3^{+9.2}_{-9.2}$	0.21
R5 (South)	$3.27^{+0.23}_{-0.21}$	$3.26^{+0.10}_{-0.13}$	$25.4^{+1.2}_{-1.2}$	$68.8^{+8.9}_{-9.2}$	185^{+11}_{-12}	$33.7^{+5.2}_{-5.2}$	0.43
R2 to R4 (North)	$5.52^{+0.15}_{-0.15}$	$3.35^{+0.06}_{-0.06}$	$89.3^{+2.6}_{-2.6}$	161^{+13}_{-12}	660^{+24}_{-24}	120^{+17}_{-17}	0.64
R2 to R5 (Outer Regions)	$4.88^{+0.13}_{-0.12}$	$3.33^{+0.05}_{-0.05}$	111^{+3}_{-3}	225^{+15}_{-15}	821^{+26}_{-25}	149^{+22}_{-22}	0.83

[a] see Sect. 2.3

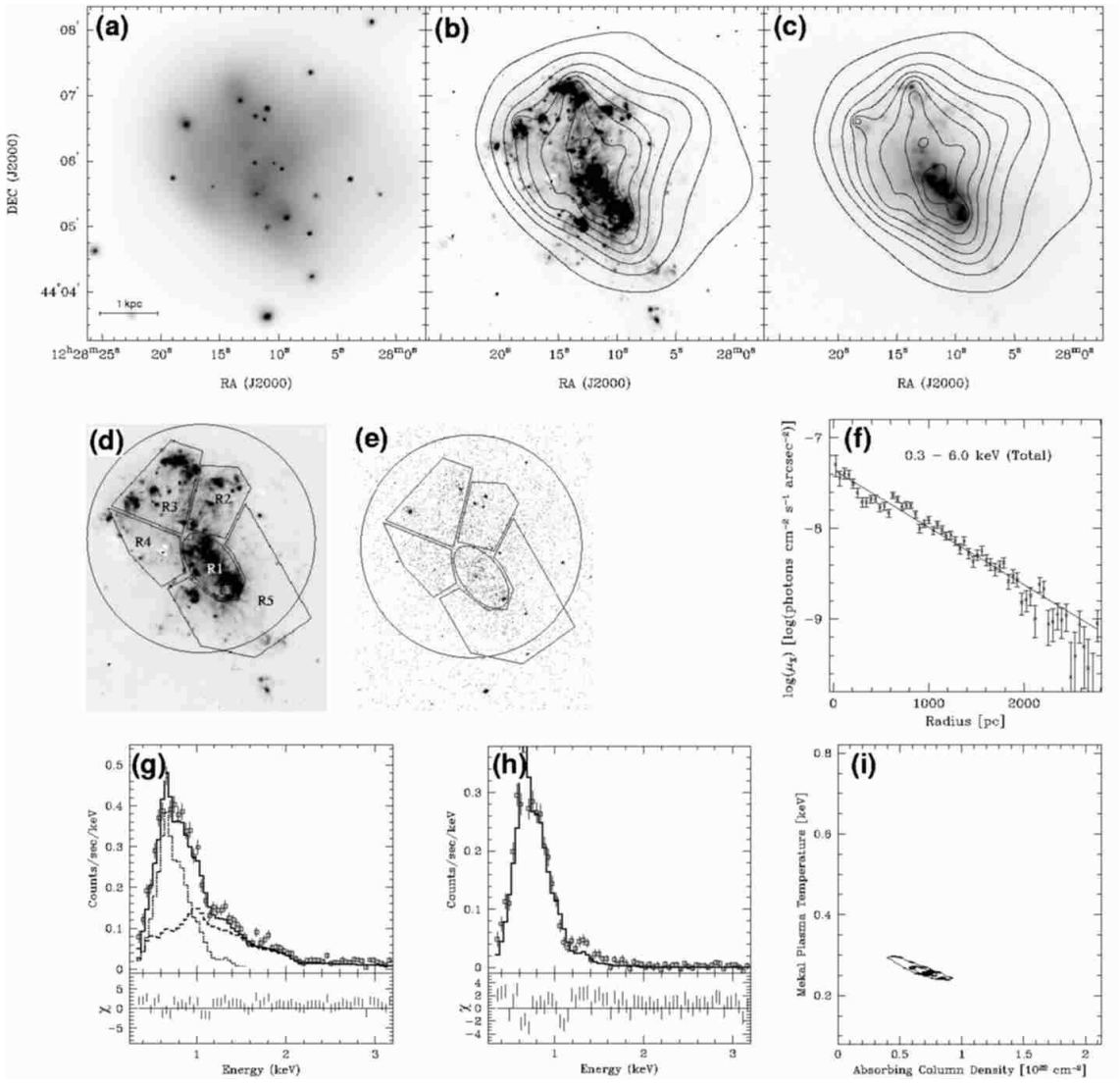

Figure 9. Images and spectra for the X-ray emission of NGC 4449. See the caption of Fig. 3 for details. The contours of the logarithmic X-ray emission in panels (b) and (c) are spaced by $0.1\log(peakflux)$ starting at $0.2\log(peakflux)$ (continuum subtracted Hα image taken from Bomans, Chu & Hopp 1997; Optical Lowell 1.1m R–band image from Frei et al. 1996).

model with $T = 3.2$ and 10×10^6 K to the diffuse component and estimate its mass to $\sim 10^7\,M_\odot$. Some of the hot gas was detected in the interior of an expanding superbubble visible in Hα. They also attribute 28 X-ray point sources to NGC 4449.

4.6.2 Chandra observations revisited

With a size of $8\farcm9 \times 9\farcm2$ (corresponding to 10.0 kpc $\times$10.4 kpc) the diffuse X-ray distribution of NGC 4449 is impressively large. Its morphology is similar to the Hα distribution of NGC 4449 (see Fig. 9[b]). To the west, however, the X-ray emission is more extended. We detect 18 point sources in NGC 4449 (see Fig. 10[a]). With a count rate of ~ 0.05 cnts s^{-1} P17 is the strongest, followed by P6 and P9 (see Table 19). The latter source was previously classified as a SNR (see above). In Figs. 10(b) and 10(c) we plot a hardness ratio diagram of all the point sources. Seven of the point source spectra are well fit by provisional thermal plasma MeKaL models (P2, P7, P9, P11, P12, P14, P16) and nine by power laws (P1, P3, P4, P5, P6, P10, P13, P15, P17). To select which emission model provides the best fit, the location of the sources in the hardness ratio plots was equally taken into account. In addition, we detect two super-soft sources (P8 and P18), one near the centre of NGC 4449 and another one further out. Individual, final fits to the spectra with sufficient counts are shown in Fig. 10(d) and the fitted parameters are given in Table 20. Due to crowding and absorption effects, an unambiguous cross identification of X-ray point sources with optical counterparts within the *HST*/WFPC2 field (see Fig. 10[a]) is not possible.

The azimuthally averaged X-ray surface brightness profiles of NGC 4449 are well described by an exponential function with small deviations only (Fig. 9[f]). The scale length of the soft X-ray emission is with ~ 700 pc slightly smaller compared to that of the hard emission (~ 740 pc). This is not expected, since hardening of the emission due to photoelectric absorption would restrict the hard emission more to the centre. Regarding the large error of typically 90 pc in the scale length, however, this is only a tentative result. The temperature of the hot, diffuse gas in the centre of NGC 4449 is equal to the temperature in the outer regions ($\sim 3.2 \times 10^6$ K; see Figs. 9(d) and 9(e) for the definition of the regions and Fig. 9(h) and 9(i) for the fits and confidence regions of the total diffuse X-ray emission; see also Table 18 for the parameters derived). Following our analysis, we do not need to introduce a second temperature component to find a good fit to the spectra. This result suggests that the hot gas has been heated more uniformly over the disc or that the cooling time exceeds the age of the starburst. The absorbing column density of the northern half of NGC 4449 is higher than that toward the south. This leads to the conclusion that the z-axis pointing to the north is tipped towards us and hence that the disc gas absorbs the X-rays emerging from the hot gas. The southern part of the gaseous disc is located behind the hot outflow. The total diffuse unabsorbed X-ray luminosity derived from the MeKaL fit is 4.5×10^{39} erg s^{-1}. The X-ray luminosity and temperature are in good agreement with the *ROSAT* measurements (within a factor of ~ 2). Note that the *ROSAT* result was determined within an energy range of 0.1–2.0 keV and that the point source confusion of the *ROSAT* data can contribute to the difference. Adding up point sources and the the diffuse emission, the total X-ray luminosity of NGC 4449 results in 7.9×10^{40} erg s^{-1}.

4.7 NGC 5253 (UGCA 369, Haro 10, ESO 445-G 4)

4.7.1 Previous X-ray observations and results

EINSTEIN was the first X-ray observatory to detect NGC 5253 and Fabbiano, Kim & Trinchieri (1992) derived a luminosity of 7×10^{38} erg s^{-1}. Martin & Kennicutt (1995) analysed follow-up observations with the *ROSAT* PSPC instrument (35 ks). They detected an extended soft source coinciding with the galaxy's centre which they fit with a thermal plasma with a temperature of 4×10^6 K (luminosity: 6.5×10^{38} erg s^{-1}). The X-ray emission was interpreted as emerging from the interior of an Hα superbubble. In order to resolve the soft X-ray source, Strickland & Stevens (1999) observed NGC 5253 with the *ROSAT* HRI (71 ks). They detected five sources which they identified with young massive stellar clusters at the centre. Three of the sources were found to be extended and they concluded that X-rays originate in sources which are commonly associated with star forming regions, i.e., SNRs and massive XRBs (point sources) as well as superbubbles (extended sources). More recently, Summers et al. (2004) presented an analysis of *Chandra* and *XMM-Newton* data of NGC 5253. They examine in detail 17 X-ray point sources and the diffuse X-ray emission and derive an X-ray luminosity of the hot gas of $\sim 2 \times 10^{38}$ erg s^{-1} emitted by hot gas with temperatures of 2.6 and 8.2×10^6 K.

4.7.2 Chandra observations revisited

The *Chandra* data of NGC 5253 show a total of seven point sources embedded in an extended region, $1\farcm8 \times 1\farcm3$ in size (corresponding to 1.7×1.2 kpc). The area of high surface brightness, however, is less extended in the east-west direction ($1\farcm0$ or ~ 1.0 kpc) as compared to the faint emission. The distribution of the diffuse X-ray emission is similar to the Hα morphology, which also exhibits a low surface brightness extension to the west (see Fig. 11[b]). Except for the point source P1 (Fig. 12[a]), which is located toward the south-west, all X-ray point sources lie close to the centre of NGC 5253. The count rates of all point sources and their hardness ratios are listed in Table 22 and the corresponding hardness ratio plot is shown in Figs. 12(b) and (c). The fits to the spectra for the six point sources with sufficient counts are displayed in Fig. 12 and the resulting parameters are listed in Table 23. Of the seven point sources, only P1 is best modeled by a power law. All the others appear to emit line and continuum radiation due to a hot thermal plasma with temperatures of $\sim 2-4 \times 10^6$ K (P6, the strongest point source, exhibits a temperature which is about a factor of 4 higher). A highly obscured, very young super-stellar cluster resides between P4 and P5. The X-ray data are therefore in good agreement with the scenario that those X-ray point sources are members of this or neighbouring stellar clusters. No clear optical counterparts can be detected on an *HST*/WFPC2 F555W (Johnson V band) image (Fig. 12[a]).

The azimuthally averaged, X-ray surface brightness profiles of NGC 5253 in the different X-ray bands are well described by an exponential decline at least toward smaller

Table 19. Positions, count rates and hardness ratios of the point sources in NGC 4449. The Right Ascension and Declination are given in ^{h} ^{m} ^{s} and $^\circ$ $'$ $''$ (J2000), respectively. The count rates of the total, soft, medium, and hard emission are in units of 10^{-5} cts s^{-1}. See Fig. 10 for the locations of the point sources coinciding with this galaxy as well as for their distribution in a hardness ratio plot.

No.	RA	DEC	Total	Soft	Medium	Hard	HR1	HR2
P1	12 28 03.9	+44 05 43.7	511.3 ± 44.5	86.47 ± 18.80	124.1 ± 21.6	300.8 ± 34.0	-0.66 ± 0.07	-0.18 ± 0.10
P2	12 28 06.8	+44 05 27.5	90.23 ± 19.89	22.56 ± 10.63	26.32 ± 9.95	41.35 ± 13.55	-0.50 ± 0.20	$+0.08 \pm 0.25$
P3	12 28 07.2	+44 04 14.7	135.3 ± 22.6	3.76 ± 3.76	11.28 ± 6.51	120.3 ± 21.3	-0.94 ± 0.05	-0.78 ± 0.11
P4	12 28 07.3	+44 07 21.1	300.8 ± 34.0	37.59 ± 11.89	71.43 ± 17.23	191.7 ± 26.8	-0.75 ± 0.07	-0.28 ± 0.12
P5	12 28 07.3	+44 04 53.8	594.0 ± 48.1	191.7 ± 27.4	199.3 ± 28.4	203.0 ± 27.6	-0.35 ± 0.08	$+0.32 \pm 0.09$
P6	12 28 09.3	+44 05 08.1	4417 ± 129	1132 ± 65	1338 ± 71	1947 ± 86	-0.49 ± 0.03	$+0.12 \pm 0.03$
P7	12 28 09.7	+44 05 53.1	736.9 ± 55.3	67.67 ± 19.89	142.9 ± 23.8	526.3 ± 45.7	-0.82 ± 0.05	-0.43 ± 0.08
P8	12 28 10.4	+44 05 58.0	172.9 ± 29.1	157.9 ± 26.6	11.28 ± 9.95	3.76 ± 6.51	$+0.83 \pm 0.13$	$+0.96 \pm 0.07$
P9	12 28 11.0	+44 06 48.4	3793 ± 120	424.8 ± 40.0	1545 ± 77	1823 ± 83	-0.78 ± 0.02	$+0.04 \pm 0.04$
P10	12 28 11.0	+44 04 59.4	127.8 ± 24.4	18.80 ± 9.95	22.56 ± 13.02	86.47 ± 18.03	-0.71 ± 0.14	-0.35 ± 0.22
P11	12 28 11.2	+44 06 38.1	402.3 ± 40.7	127.8 ± 22.6	157.9 ± 26.0	116.5 ± 21.6	-0.36 ± 0.09	$+0.42 \pm 0.12$
P12	12 28 11.9	+44 05 29.7	218.0 ± 36.1	15.04 ± 15.95	67.67 ± 21.27	135.3 ± 24.4	-0.86 ± 0.14	-0.24 ± 0.23
P13	12 28 12.0	+44 06 41.5	699.3 ± 53.4	109.0 ± 22.2	248.1 ± 32.3	342.1 ± 36.3	-0.69 ± 0.06	$+0.02 \pm 0.10$
P14	12 28 12.1	+44 05 58.5	233.1 ± 32.3	56.39 ± 15.50	105.3 ± 23.2	71.43 ± 16.39	-0.52 ± 0.12	$+0.39 \pm 0.18$
P15	12 28 13.3	+44 06 55.6	954.9 ± 61.8	142.9 ± 25.5	315.8 ± 36.1	496.2 ± 43.2	-0.70 ± 0.05	-0.04 ± 0.08
P16	12 28 15.6	+44 05 36.8	75.19 ± 17.63	33.84 ± 11.29	30.08 ± 11.89	11.29 ± 6.51	-0.10 ± 0.23	$+0.70 \pm 0.25$
P17	12 28 17.8	+44 06 33.6	5222 ± 141	86.47 ± 20.25	755.6 ± 54.1	4380 ± 129	-0.97 ± 0.01	-0.68 ± 0.02
P18	12 28 19.1	+44 05 44.4	161.7 ± 24.7	157.9 ± 24.4	3.76 ± 3.76	0.00 ± 0.00	$+0.95 \pm 0.05$	$+1.00 \pm 0.01$

Table 20. Parameters of the fitted X-ray emission models to the point sources in NGC 4449. See the caption of Table 11 for details and Fig. 10(d) for the individual spectra and fits. The last column displays the numbering scheme of Summers et al. (2003).

No.	Model	N_H [10^{21} cm^{-2}]	T/γ [10^6 K/–]	$Norm/Ampl^a$ [10^{-5}]	$F_{\rm X}^{\rm abs}$ [10^{-15} erg s^{-1} cm^{-2}]	$F_{\rm X}$	$L_{\rm X}$ [10^{37} erg s^{-1}]	Cross Ident. No.
P1	PL	3.44	1.85	0.66	32.66	44.38	8.08	5
P5	PL	5.77	3.72	1.02	14.58	119.5	21.75	9
P6	PL	6.63	3.08	11.05	170.6	791.6	144.1	10
P7	MEK	5.34	40.5	4.33	42.67	61.01	11.10	11
P8	BB	11.36	0.32	2e10	2.67	35000	6370	12
P9	MEK	6.20	12.78	26.54	122.6	265.8	48.38	15
P11	MEK	0.79	12.53	1.39	11.19	13.97	2.54	17
P12	MEK	6.22	4.69	1.70	4.09	14.84	2.70	19
P13	PL	15.45	5.04	5.11	18.78	2361	429.7	20
P14	MEK	1.58	10.01	0.87	6.24	8.95	1.63	21
P15	PL	9.32	3.35	3.32	36.22	285.9	52.03	23
P17	PL	16.07	2.16	20.42	519.9	1195	217.5	27
P18	BB	9.67	0.58	5.4e6	3.83	1024	186.4	28

[a] see Sect. 2.3

Table 21. Results of MeKaL collisional thermal plasma model fits applied to the X-ray spectra of different regions in NGC 5253 (see panels [d] and [e] in Fig. 11 for the definition of the regions).

Region	$N_{\rm H}$ [10^{21} cm^{-2}]	T [10^6 K]	$Norm^a$ [10^{-5}]	$F_{\rm X}^{\rm abs}$ [10^{-15} erg s^{-1} cm^{-2}]	$F_{\rm X}$ [10^{-15} erg s^{-1} cm^{-2}]	$L_{\rm X}$ [10^{37} erg s^{-1}]	χ^2_{red}
Total	$5.67^{+0.23}_{-0.22}$	$3.51^{+0.08}_{-0.08}$	$55.5^{+2.0}_{-2.1}$	$81.6^{+8.6}_{-8.1}$	359^{+18}_{-17}	$46.6^{+7.0}_{-7.0.}$	0.64
R1 (Centre)	$10.1^{+0.3}_{-0.3}$	$3.79^{+0.09}_{-0.09}$	$44.6^{+2.0}_{-2.0}$	$39.3^{+5.0}_{-4.6}$	299^{+17}_{-17}	$38.9^{+5.9}_{-5.9}$	0.23
R2 (West)	$11.4^{+1.1}_{-0.9}$	$2.62^{+0.16}_{-0.17}$	$22.0^{+3.8}_{-3.8}$	$7.79^{+4.36}_{-3.27}$	124^{+25}_{-25}	$16.1^{+4.0}_{-4.0}$	0.34
R3 (North)	$0.90^{+0.88}_{-0.74}$	$5.48^{+0.89}_{-1.01}$	$2.09^{+0.29}_{-0.29}$	$10.4^{+4.4}_{-3.9}$	$17.1^{+3.7}_{-3.9}$	$2.23^{+0.59}_{-0.59}$	0.40
R4 (South)	$6.69^{+0.61}_{-0.55}$	$3.10^{+0.16}_{-0.16}$	$13.6^{+1.4}_{-1.4}$	$14.2^{+4.2}_{-3.6}$	$82.5^{+10.4}_{-9.9}$	$10.7^{+2.1}_{-2.1}$	0.36
R3+R4	$6.69^{+0.67}_{-0.60}$	$3.28^{+0.20}_{-0.18}$	$18.6^{+2.0}_{-2.0}$	$21.2^{+6.8}_{-5.6}$	116^{+16}_{-15}	$15.1^{+3.0}_{-3.0}$	0.45
R2 to R4 (Outer Regions)	$7.58^{+0.88}_{-0.75}$	$3.21^{+0.23}_{-0.19}$	$25.6^{+3.4}_{-3.4}$	$24.6^{+10.1}_{-7.8}$	158^{+27}_{-25}	$20.6^{+4.6}_{-4.6}$	0.49

[a] see Sect. 2.3

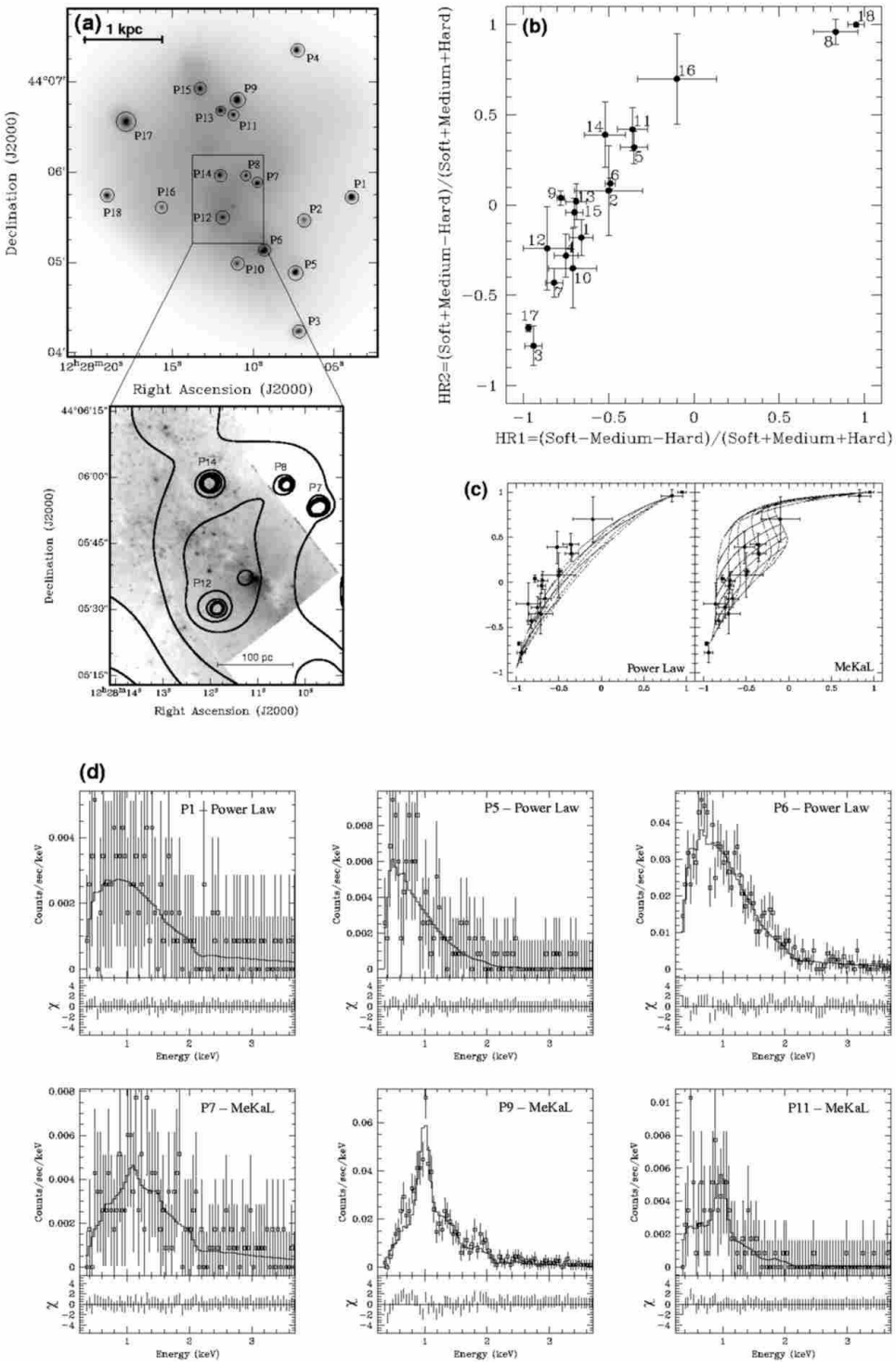

Figure 10. Locations and spectra of the point sources in NGC 4449. See caption of Fig. 4 for details. The count rates, hardness ratios and fit parameters are listed in Tables 19 and 20.

radii; at large radii the profiles level off (Fig. 11[f]). We derive the soft emission to be more extended ($h_{Soft} \simeq 150$ pc, see Table 9) compared to the hard emission (~ 70 pc). The strong optical absorption feature to the east of NGC 5253 is in agreement with the detection of dust lanes and molecular complexes at that position (see, e.g., Meier, Turner & Beck 2002). This absorption is also evident in diffuse X-rays; not only the surface brightness is lower at this location but the emission is also considerably harder than the emission toward the north and south. Fits of thermal plasma models to individual regions in NGC 5253 (see Fig. 11[d] and [e]) reveal that temperatures of the hot gas are very sim-

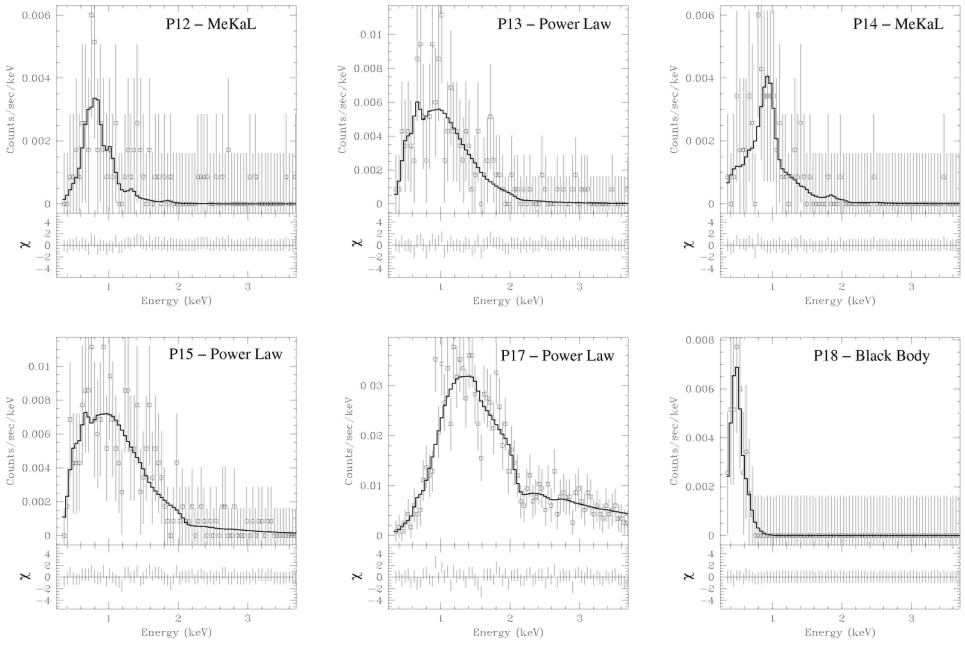

Figure 10. continued.

ilar for all areas ($T \simeq 3 \times 10^6$ K; Table 21 and Fig. 11[h] and [i] for the model fits and the confidence regions to the overall emission). The absorbing column density in the centre ($N_{\rm H} \simeq 10^{22}\,{\rm cm}^{-2}$), however, is larger than that of the other regions (in agreement with the observed dust lanes and molecular complexes). The fit to the northern part of NGC 5253 results in a very low value of $N_{\rm H} \lesssim 10^{20}\,{\rm cm}^{-2}$, whereas the southern part is absorbed by a column density which is about a factor of 10 higher. We conclude that the south of the disc of NGC 5253 is located between the hot gas and the observer, whereas the northern part of the cool disc gas lies behind the hot wind. The total diffuse X-ray luminosity is 4.7×10^{38} erg s^{-1}. The temperature of the hot gas agrees well with previous *ROSAT* observations. Adding up the X-ray luminosities of the point sources and of the hot gas (total X-ray luminosity: 1.9×10^{39} erg s^{-1}) the *ROSAT* and *Chandra* results are almost identical (see Fig. 11[g]).

4.8 He 2-10 (ESO 495-G 21)

4.8.1 Previous X-ray observations and results

Stevens & Strickland (1998) analysed 9.2 ks of *ROSAT* PSPC observations of He 2-10. They detected a point-like source and fitted a single temperature RS plasma with a temperature of $\sim 5 \times 10^6$ K and a luminosity of 10^{40} erg s^{-1} to its spectrum. Méndez et al. (1999) published a multi-wavelength analysis of He 2-10 including the *ROSAT* PSPC and new HRI (38 ks) observations. Based on a correlation analysis with Hα maps they conclude that hot gas fills a bipolar superbubble. Furthermore, they speculate that there is an outflow of hot gas and that part of it can escape the galaxy's gravitational potential.

4.8.2 Chandra observations

The total X-ray emission of He 2-10 is approximately circularly shaped and has a diameter of 1.′7 (4.4 kpc). Within the diffuse X-ray emission and the optical and Hα counterpart we detect five point sources: three of them are at the same position as the central star forming complex (P1, P2, P3) and one is located close to the eastern complex (P4; see Fig 14[a]). The fifth source is placed further away to the east and is slightly shifted to the north (P5). P1 is the strongest of the sources, followed by P2 (see Table 25 for positions, count rates, and hardness ratios of the point source population). P3 coincides with the brightest radio continuum source detected by Kobulnicky & Johnson (1999) (their knot 4) and shows a radio spectrum indicative of an optically thick thermal bremsstrahlung origin. P1 coincides with their knot 3 and exhibits a flat radio continuum spectrum. A hardness ratio plot of all X-ray point sources is shown in Figs. 14(b) and (c) and individual spectra are displayed in Fig. 14(d). The fitted parameters for point sources with sufficient counts are listed in Table 26. P2, P3, and P4 are best fit by a collisional thermal plasma, whereas P1 is in better agreement with a power law function. All fits to P1, however, are unsatisfactory and a more sophisticated model may be needed to reach a more acceptable result. Given the large distance to He 2-10, only the most luminous sources are detected. They exceed luminosities of 10^{39} erg s^{-1} which puts them in the range of ULXs.

The shape of the underlying diffuse X-ray emission basically follows the Hα morphology of He 2-10 (see Fig. 13[b]). The azimuthally averaged X-ray surface brightness profiles are similar to those of NGC 5253: the soft emission has a much larger exponential scale length ($\sim$ 320 pc, Table 9) than the hard emission ($\sim$ 150 pc). In addition, at large radii the profile levels off (see Fig. 13[f]). The central temperature of the hot gas ($T \sim 7.6 \times 10^6$ K) is higher than

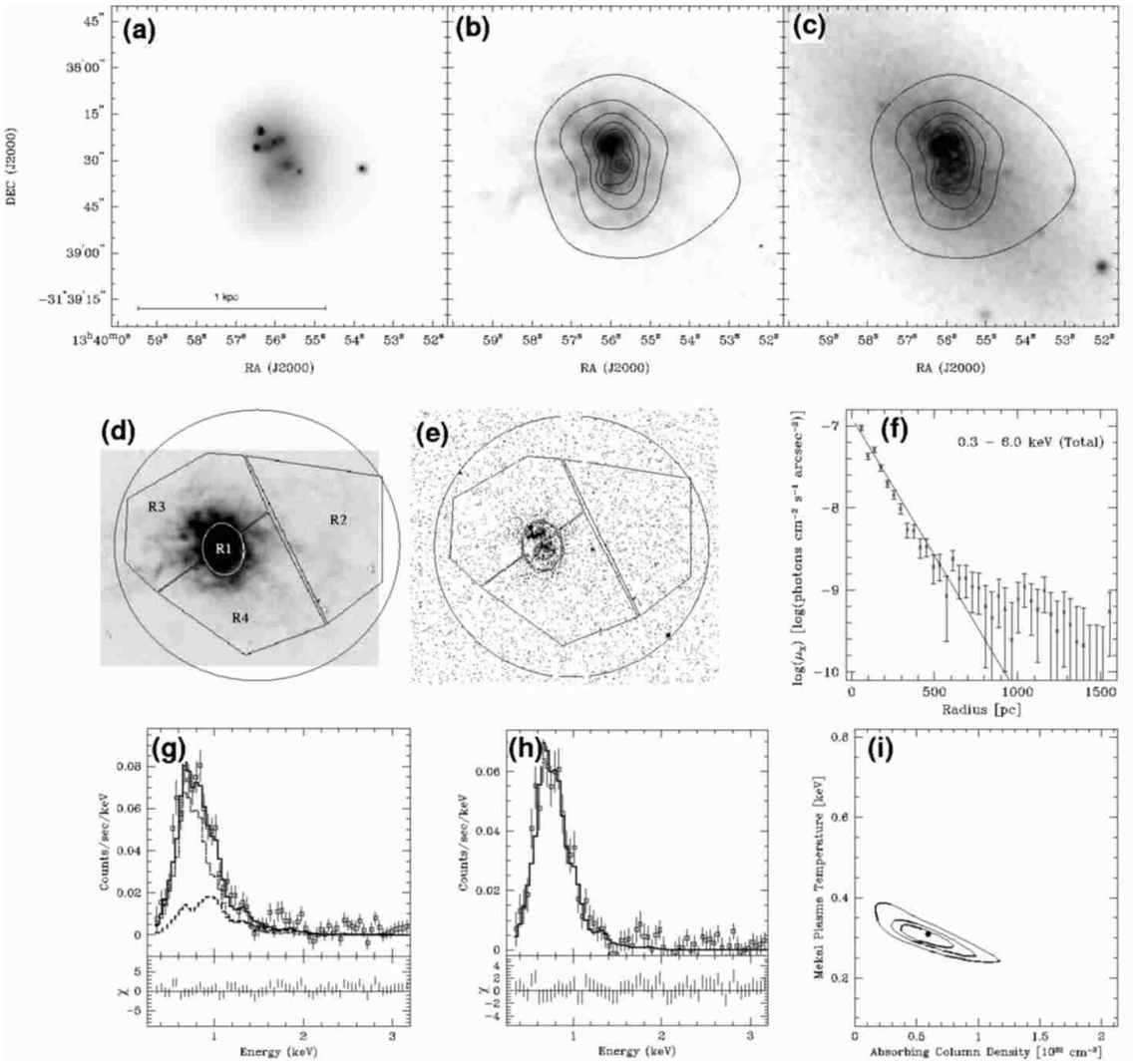

Figure 11. Images and spectra for the X-ray emission of NGC 5253. See the caption of Fig. 3 for details (continuum subtracted Hα image taken from Martin 1998, the optical *R*–band 1.1m ESO Schmidt image from Lauberts & Valentijn 1989).

Table 22. Positions, count rates and hardness ratios of the point sources in NGC 5253. The Right Ascension and Declination are given in ^{h} ^{m} ^{s} and $^\circ$ $'$ $''$ (J2000), respectively. The count rates of the total, soft, medium, and hard emission are in units of 10^{-5} cts s^{-1}. See Fig. 12 for the locations of the point sources coinciding with this galaxy as well as for their distribution in a hardness ratio plot.

No.	RA	DEC	Total	Soft	Medium	Hard	HR1	HR2
P1	13 39 53.8	−31 38 32.9	64.45 ± 12.51	11.72 ± 5.52	19.53 ± 7.31	33.20 ± 8.51	-0.64 ± 0.15	-0.03 ± 0.24
P2	13 39 55.4	−31 38 33.7	85.94 ± 16.12	31.25 ± 9.57	39.06 ± 10.70	15.63 ± 7.31	-0.27 ± 0.18	$+0.64 \pm 0.22$
P3	13 39 55.7	−31 38 31.6	97.21 ± 15.68	23.37 ± 7.32	48.58 ± 11.26	25.26 ± 8.08	-0.52 ± 0.13	$+0.48 \pm 0.21$
P4	13 39 55.9	−31 38 23.7	91.80 ± 17.04	11.12 ± 7.47	55.89 ± 12.32	24.79 ± 9.09	-0.76 ± 0.15	$+0.46 \pm 0.28$
P5	13 39 56.0	−31 38 24.3	131.3 ± 18.3	19.73 ± 6.71	61.96 ± 12.90	49.64 ± 11.09	-0.70 ± 0.10	$+0.24 \pm 0.19$
P6	13 39 56.4	−31 38 20.7	830.8 ± 41.3	74.43 ± 12.92	338.2 ± 26.40	418.2 ± 29.0	-0.82 ± 0.03	-0.01 ± 0.06
P7	13 39 56.5	−31 38 25.9	180.5 ± 20.3	62.34 ± 11.42	91.31 ± 14.29	26.86 ± 8.85	-0.31 ± 0.10	$+0.70 \pm 0.14$

that of the outer regions ($T \sim 3.5 \times 10^6$ K, see Fig. 13[d] and [e] for the definitions of the regions and Table 24 for the fit results). Based on the fitted absorbing column densities, the orientation of the disc of He 2-10 is such that the north and east of the disc is directed away from us (the hot gas being in front of the disc) while the south and the west is more absorbed and the disc is therefore pointing toward the observer. The total X-ray luminosity of the diffuse emission is equal to 2×10^{40} erg s^{-1}. Adding up the diffuse plus the point source X-ray luminosities yields 8.1×10^{40} erg s^{-1}. The thermal plasma results agree within a factor of ~ 2 with the *ROSAT* results.

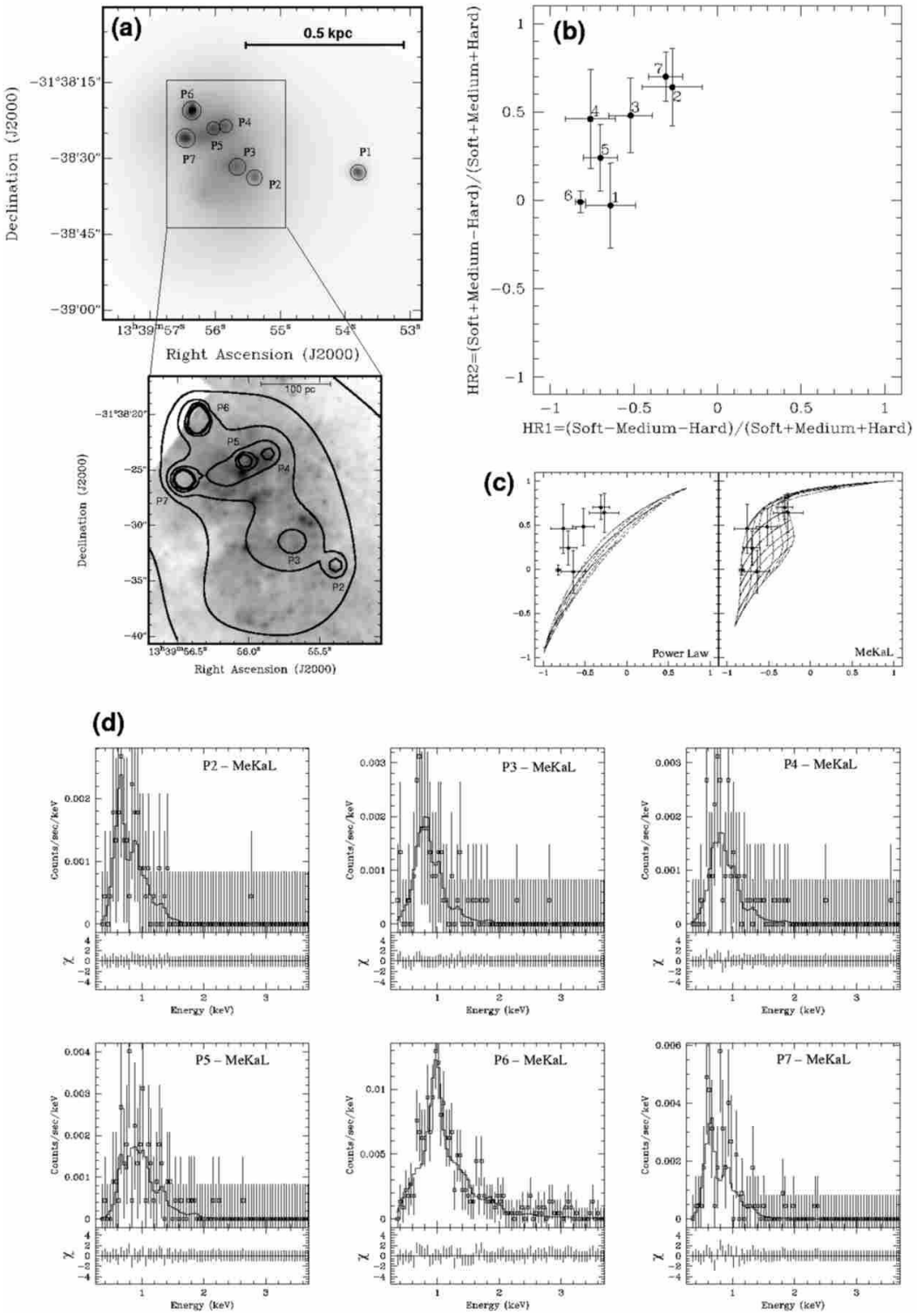

Figure 12. Locations and spectra of the point sources in NGC 5253. See caption of Fig. 4 for details. The count rates, hardness ratios and fitted parameters are listed in Tables 22 and 23.

Table 23. Parameters of the fitted X-ray emission models to the point sources in NGC 5253. See the caption of Table 11 for details and Fig. 12(d) for the individual spectra and fits.

No.	Model	N_H	T/γ	$Norm/Ampl^a$	$F_{\rm X}^{\rm abs}$	$F_{\rm X}$	$L_{\rm X}$
		$[10^{21}\,{\rm cm}^{-2}]$	$[10^6\,{\rm K}/-]$	$[10^{-5}]$	$[10^{-15}\,{\rm erg\,s^{-1}\,cm^{-2}}]$		$[10^{37}\,{\rm erg\,s^{-1}}]$
P2	MEK	19.78	2.03	61.22	2.46	285.2	37.08
P3	MEK	6.79	4.73	1.42	2.55	10.74	1.40
P4	MEK	9.37	4.00	2.20	2.27	15.20	1.98
P5	MEK	22.23	2.87	27.89	3.17	163.6	21.27
P6	MEK	5.35	12.04	5.90	24.97	54.77	7.12
P7	MEK	19.77	1.80	136.2	3.47	557.6	72.49

[a] see Sect. 2.3

Table 24. Results of MeKaL collisional thermal plasma model fits applied to the X-ray spectra of different regions in He 2–10 (see panels [d] and [e] in Fig. 13 for the definition of the regions).

Region	$N_{\rm H}$	T	$Norm^a$	$F_{\rm X}^{\rm abs}$	$F_{\rm X}$	$L_{\rm X}$	χ^2_{red}
	$[10^{21}\,{\rm cm}^{-2}]$	$[10^6\,{\rm K}]$	$[10^{-5}]$	$[10^{-15}\,{\rm erg\,s^{-1}\,cm^{-2}}]$	$[10^{-15}\,{\rm erg\,s^{-1}\,cm^{-2}}]$	$[10^{37}\,{\rm erg\,s^{-1}}]$	
Total	$4.44^{+0.35}_{-0.29}$	$2.82^{+0.14}_{-0.14}$	$93.6^{+13.0}_{-13.0}$	103^{+46}_{-36}	2101^{+319}_{-313}	2038^{+423}_{-423}	0.32
R1 (Centre)	$1.23^{+0.22}_{-0.20}$	$7.60^{+0.44}_{-0.44}$	$3.38^{+0.27}_{-0.27}$	$41.9^{+6.9}_{-6.5}$	$95.6^{+6.3}_{-6.4}$	$92.7^{+14.5}_{-14.5}$	0.09
R2 (West)	$2.11^{+0.29}_{-0.25}$	$3.21^{+0.22}_{-0.21}$	$3.91^{+0.53}_{-0.53}$	$15.4^{+6.2}_{-5.2}$	$91.4^{+14.5}_{-13.7}$	$88.7^{+18.2}_{-18.2}$	0.06
R3 (South)	$3.19^{+0.38}_{-0.31}$	$2.89^{+0.20}_{-0.20}$	$5.60^{+0.95}_{-0.95}$	$11.0^{+6.0}_{-4.5}$	128^{+24}_{-23}	124^{+29}_{-29}	0.05
R4 (East)	$0.00^{+0.29}_{-0.00}$	$7.44^{+0.72}_{-0.73}$	$0.94^{+0.13}_{-0.13}$	$17.7^{+2.4}_{-4.0}$	$26.5^{+3.0}_{-3.1}$	$25.7^{+4.7}_{-4.7}$	0.09
R5 (North)	$0.68^{+0.71}_{-0.52}$	$5.14^{+1.41}_{-1.07}$	$0.45^{+0.12}_{-0.12}$	$5.65^{+4.40}_{-3.22}$	$12.4^{+4.2}_{-4.2}$	$12.0^{+4.4}_{-4.4}$	0.05
R2+R4	$2.68^{+0.19}_{-0.17}$	$3.21^{+0.12}_{-0.13}$	$10.3^{+0.9}_{-0.9}$	$31.3^{+7.7}_{-7.1}$	240^{+24}_{-23}	232^{+40}_{-40}	0.16
R3+R5	$1.65^{+0.29}_{-0.25}$	$3.83^{+0.33}_{-0.31}$	$2.94^{+0.37}_{-0.37}$	$18.3^{+7.1}_{-5.8}$	$72.4^{+11.6}_{-10.8}$	$70.2^{+14.9}_{-14.9}$	0.08
R2 to R5 (Outer Regions)	$2.82^{+0.15}_{-0.14}$	$3.21^{+0.11}_{-0.10}$	$17.5^{+1.2}_{-1.2}$	$50.4^{+9.9}_{-9.1}$	410^{+32}_{-31}	397^{+64}_{-64}	0.22

[a] see Sect. 2.3

Table 25. Positions, count rates and hardness ratios of the point sources in He 2-10. The Right Ascension and Declination are given in $^h\ ^m\ ^s$ and $^\circ\ '\ ''$ (J2000), respectively. The count rates of the total, soft, medium, and hard emission are in units of 10^{-5} cts s^{-1}. See Fig. 14 for the locations of the point sources coinciding with this galaxy as well as for their distribution in a hardness ratio plot.

No.	RA	DEC	Total	Soft	Medium	Hard	HR1	HR2
P1	08 36 15.105	−26 24 33.56	1209 ± 84	74.47 ± 22.41	225.6 ± 42.1	908.8 ± 69.2	-0.88 ± 0.04	-0.50 ± 0.07
P2	08 36 15.252	−26 24 34.67	853.5 ± 71.6	97.54 ± 25.04	384.7 ± 49.4	371.3 ± 45.4	-0.77 ± 0.05	$+0.13 \pm 0.12$
P3	08 36 15.380	−26 24 33.56	260.5 ± 39.6	39.81 ± 16.23	94.14 ± 25.73	126.5 ± 25.3	-0.69 ± 0.11	$+0.03 \pm 0.20$
P4	08 36 15.838	−26 24 34.30	266.7 ± 40.7	10.63 ± 9.88	63.26 ± 23.22	192.8 ± 31.9	-0.92 ± 0.07	-0.45 ± 0.18
P5	08 36 16.048	−26 24 30.98	131.6 ± 25.8	5.06 ± 5.06	35.43 ± 13.39	91.10 ± 21.47	-0.92 ± 0.08	-0.38 ± 0.21

Table 26. Parameters of the fitted X-ray emission models to the point sources in He 2-10. See the caption of Table 11 for details and Fig. 14(d) for the individual spectra and fits.

No.	Model	N_H	T/γ	$Norm/Ampl^a$	$F_{\rm X}^{\rm abs}$	$F_{\rm X}$	$L_{\rm X}$
		$[10^{21}\,{\rm cm}^{-2}]$	$[10^6\,{\rm K}/-]$	$[10^{-5}]$	$[10^{-15}\,{\rm erg\,s^{-1}\,cm^{-2}}]$		$[10^{37}\,{\rm erg\,s^{-1}}]$
P1	PL	0.00	1.00	0.90	147.4	155.4	150.7
P2	MEK	8.41	2.06	297.5	23.09	5779	5606
P3	MEK	5.56	2.11	14.18	3.47	279.1	270.7
P4	MEK	6.78	3.46	4.63	4.01	110.5	107.2

[a] see Sect. 2.3

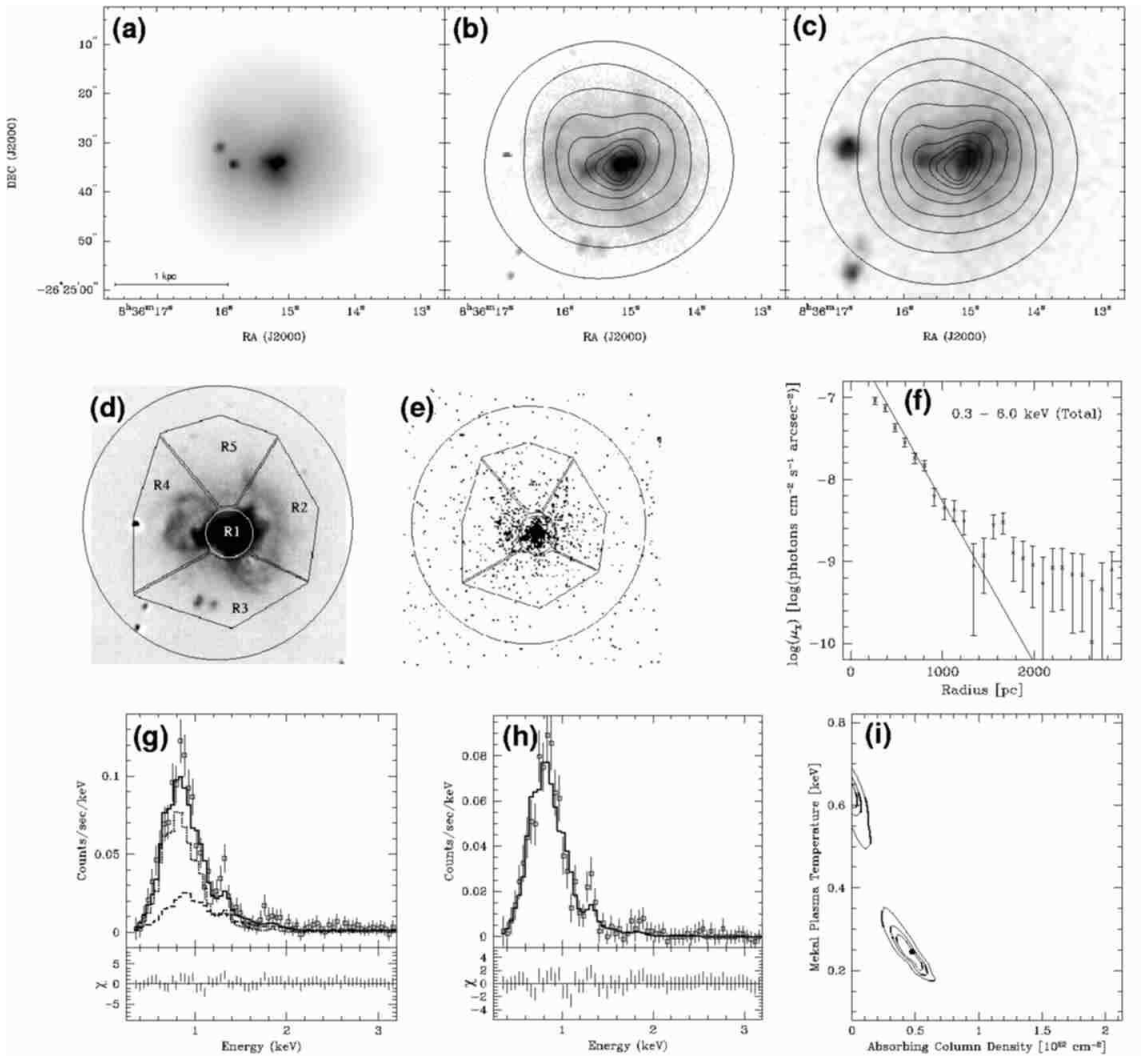

Figure 13. Images and spectra for the X-ray emission of He 2-10. See the caption of Fig. 3 for details. The contours of the logarithmic X-ray emission in panels (b) and (c) are spaced by $0.1\log(peakflux)$ and start at $0.2\log(peakflux)$ level (continuum subtracted Hα image taken from Martin 1998; the optical R–band 1.1m ESO Schmidt image is from Lauberts & Valentijn 1989).

4.9 Metallicities and α/Fe Abundances of the hot, coronal gas

In order to investigate how sensitive the model fits are to a change in metallicity (but preserving a solar element mixture as given by Anders & Grevesse 1989) we ran MeKaL fits to the emission of the targets as a whole and varied the metallicity from 0.01 to 10 times solar. The absorbing column densities, temperatures, and normalisations of the hot thermal plasmas were free parameters for these fits. The goodness-of-fit measure χ^2_{red} as a function of metallicity relative to the metallicities of the galaxies are plotted in Fig. 15 (galaxy metallicities are derived from oxygen abundances measured for H II regions within the objects [Table 4]). Except for NGC 4449 all fits deteriorate for any metallicity other than that of their H II regions. High–metallicity fits may still be acceptable for all galaxies but NGC 1569 and NGC 4449. Metallicities below $\sim$ 5% solar as, e.g., found in the massive starburst galaxy NGC 253 (Strickland et al. 2002) can be excluded for all objects but NGC 4214 and NGC 3077. Any real improvement over the fits with the H II region metallicity are only obtained for NGC 4449 which is fitted best assuming a metallicity of $\sim$ 10% solar.

Theoretical models predict that the element *mixture* of galactic winds differs from that in the solar neighbourhood. In general, the metal enrichment of the interstellar/intergalactic medium is mainly provided by SNe. The main contributors of α elements are type II SNe whereas Fe elements are overwhelmingly synthesised in type Ia SNe. The evolution of the stars involved in a SN Ia causes a substantial time delay (see, e.g., Matteucci & Recchi 2001) between type II and type Ia SNe. For this reason, the hot gas observed in a starburst should exhibit an α to Fe element abundance ratio (α/Fe) larger than unity in solar units (see, e.g., theoretical calculations by Silich et al. 2001). The determination of this ratio is difficult as the results of the spectral fitting process have quite large error bars. In spite of this challenge, we performed MeKaL fits to determine α/Fe in four ways: (a) all parameters (α and Fe element abundances, $N_{\rm H}$, T, and $Norm$) were free, (b) the α element abundances were fixed to the oxygen abundances measured on the H II

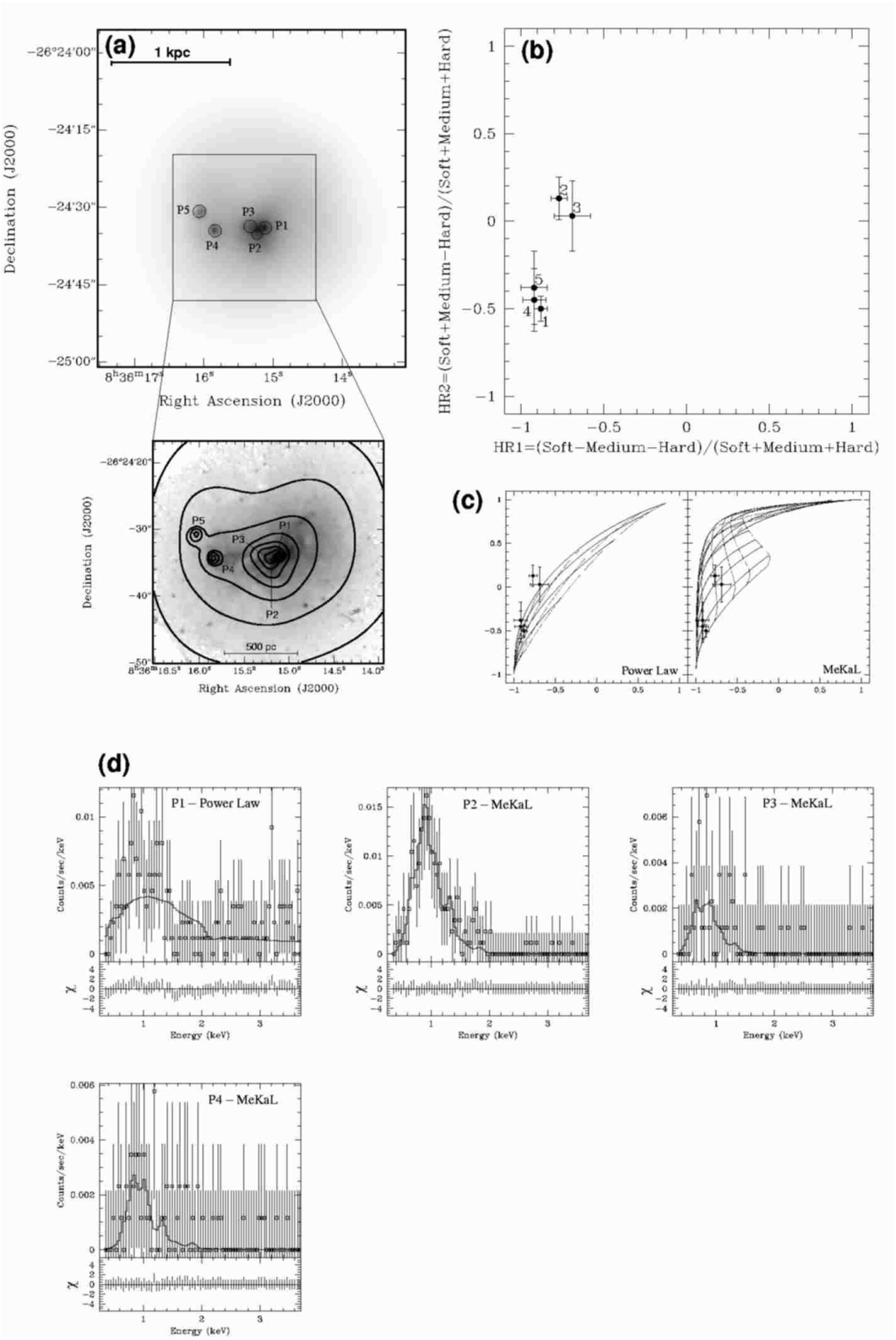

Figure 14. Locations and spectra of the point sources in He 2-10. See caption of Fig. 4 for details. The count rates, hardness ratios and fit parameters are listed in Tables 25 and 26.

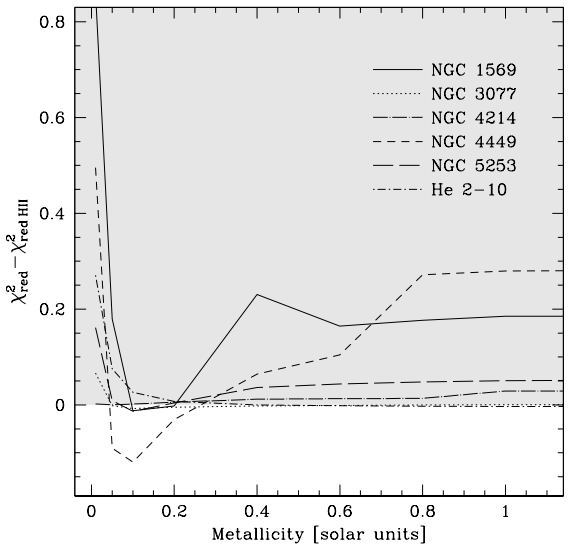

Figure 15. The goodness–of–fit indicator $\chi^2_{\rm red}$ of MeKaL fits with varying metallicity relative to fits with the galaxies' metallicities ($\chi^2_{\rm redHII}$; metallicities derived from oxygen abundances of H II regions within the objects; see Table 4). Whenever the graph is within the grey area the fits are worse than those using the galaxies' H II region metallicities, i.e., $\chi^2_{\rm red} > \chi^2_{\rm redHII}$; in the white area the fits are improved ($\chi^2_{\rm red} < \chi^2_{\rm redHII}$).

regions of the galaxies, (c) freezing $N_{\rm H}$, T, and $Norm$ to the values obtained for an α/Fe of unity but leaving the α and Fe element abundances free, and (d) only treating the Fe element abundances as a free parameter. The results as well as the corresponding $\Delta\chi^2_{\rm red} = \chi^2_{\rm red} - \chi^2_{\rm redHII}$ (reduced χ^2 relative to the fixed element mixture based on H II region metallicity) are shown in Table 27. The improved parameters resulting from methods (a) and (b) are listed in Table 28. In Table 27 the results of F–tests are also provided which were computed as models for (a) to (d) being nested (i.e., they have the same but fewer free parameters) in the model with an $\alpha/Fe = 1$ and overall metallicity fixed to the galaxies' H II region oxygen abundances. Using the 95% criterion indicates that all fits with 'F–test'< 0.05 are better than those with $\alpha/Fe = 1$. Method (d) led to α/Fe of about unity which is understandable given that the fixed parameters were obtained with exactly this assumption. With very few exceptions, α/Fe is determined to be in the range 1.3–2.7 in agreement with α element enrichment. The exceptions are NGC 3077 and NGC 4214. As discussed in Ott, Martin & Walter (2003), the hot gas in NGC 3077 is still stored in hot superbubbles whereas all the other galaxies in the sample show outflow features (see Sect. 7 in Paper II). This might be reflected in its α/Fe value of 1 but would contradict the reduced mass-loading of surrounding material (with a solar α/Fe) which is derived for NGC 3077 in Sect. 5.7 of Paper II. The number of detected X-ray photons in NGC 4214 is relatively low (only 10 ks of integration time) and methods (c) and (d) did not converge. Methods (a) and (b) led to results with very large uncertainties for NGC 4214, the best results of which are actually $\alpha/Fe < 1$. All fits were conducted using MeKaL thermal plasma models. Very similar results were obtained when we applied RS and APEC (Smith et al. 2001) models. Again, NGC 4214 is very poorly fitted, the α/Fe ratio of the hot gas stored in NGC 3077 results in about unity and the ratios for all the other galaxies are ~ 2. In summary, regarding the $\Delta\chi^2_{red}$ and the F–test results, an α element enhancement is significant for NGC 1569, NGC 4449, and He 2–10, but are not statistically supported for NGC 3077, NGC 4214, and NGC 5253. The fits result in $\alpha/Fe \sim 2$ for NGC 1569, NGC 4449, NGC 5253, and He 2–10, and $\alpha/Fe \sim 1$ for NGC 3077. The data quality of NGC 4214 does not allow us to set any constraints.

5 SUMMARY

We present a sample of eight dwarf starburst galaxies (I Zw 18, VII Zw 403, NGC 1569, NGC 3077, NGC 4214, NGC 4449, NGC 5253, and He 2-10) observed with the *Chandra* X-ray observatory. The unique combination of high angular resolution and large collecting area of the *Chandra* X-ray observatory has proven indispensable for a proper analysis of the unresolved X-ray point sources within each field, as well as for their removal from the diffuse X-ray component. We have performed an in-depth analysis of all Chandra datasets, using the exact same analysis/methods for each dwarf galaxy and find the following:

- All galaxies in the sample had previous detections with the *ROSAT* or *EINSTEIN* satellites. The *Chandra* observations show that in addition to unresolved sources, diffuse X-ray emission due to hot (coronal) gas is present in six galaxies (NGC 1569, NGC 3077, NGC 4214, NGC 4449, NGC 5253, and He 2-10) with sizes of $1-10$ kpc. In the case of I Zw 18 and VII Zw 403 only an unresolved X-ray source is detected and an upper limit to the diffuse component is determined.
- In total 55 X-ray point sources are detected in these galaxies. Optical counterparts were only identified for a minority of sources. In general, sources with sufficient counts (35 sources) are well described by power law (14), thermal plasma (18), and black body (3) spectra. Ten of the sources in our sample exceed X-ray luminosities of 10^{39} erg s^{-1} and hence are ultraluminous X-ray sources (ULX).
- Power law indices of the corresponding X-ray point sources sources range from 1 to 4 and those sources have X-ray luminosities of up to $\sim 5\times10^{39}$ erg s^{-1}. Temperatures for X-ray point sources for which the best fit was provided by a thermal plasma model are in the range of $\sim 6-40\times10^6$ K with X-ray luminosities of up to 6×10^{40} erg s^{-1}. Sources which are fit by a black body spectrum have temperatures of $\sim 0.3-0.9\times10^6$ K with a maximum luminosity of $\sim 6\times10^{40}$ erg s^{-1}.
- For those galaxies with extended emission, most of the X-ray photons (typically $60-80$ per cent) are emitted by the diffuse component. Photons from X-ray point sources only equal the diffuse emission in the case of NGC 4214. After the removal of the point sources, a single temperature thermal plasma model with a metallicity close to that measured for H II regions is in good agreement with the data. However, the temperatures vary for different regions defined within the objects. In particular, the temperatures in the centre of the galaxies ($\sim 2-7\times10^6$ K) are in general larger than those of their outskirts ($\sim 2-3\times10^6$ K). The integrated

Table 27. Fitted parameters for the determination of α/Fe with different parameters being fixed and left free.

Method	(a)			(b)		
Fixed parameters	—			α		
Free parameters	$\alpha, Fe, N_{\rm H}, T, Norm^a$			$Fe, N_{\rm H}, T, Norm^a$		
Galaxy	α/Fe	$\Delta\chi^2_{\rm red}$	F-test	α/Fe	$\Delta\chi^2_{\rm red}$	F–test
NGC 1569	$0.51/0.19 = 2.71$	-0.20	2×10^{-9}	$0.20/0.11 = 1.82$	-0.15	9×10^{-8}
NGC 3077	$0.25/0.23 = 1.09$	±0.00	0.67	$1.00/0.98 = 1.02$	±0.00	0.96
NGC 4214	$0.03/0.05 = 0.60$	±0.00	0.01	$0.25/3.10 = 0.08$	±0.00	0.03
NGC 4449	$0.19/0.08 = 2.38$	-0.20	9×10^{-9}	$0.25/0.11 = 2.27$	-0.81	1×10^{-8}
NGC 5253	$0.20/0.09 = 2.22$	±0.00	0.24	$0.20/0.11 = 1.82$	±0.00	0.08
He 2-10	$11.03/4.52 = 2.44$	-0.05	1×10^{-7}	$1.00/0.58 = 1.72$	-0.03	2×10^{-5}
Method	(c)			(d)		
Fixed parameters	$N_{\rm H}, T, Norm^a$			α, $N_{\rm H}, T, Norm^a$		
Free parameters	α, Fe			Fe		
Galaxy	α/Fe	$\Delta\chi^2_{\rm red}$	F–test	α/Fe	$\Delta\chi^2_{\rm red}$	F–test
NGC 1569	$0.39/0.18 = 2.17$	-0.15	2×10^{-7}	$0.20/0.21 = 0.95$	$+0.15$	7×10^{-6}
NGC 3077	$1.00/1.00 = 1.00$	±0.00	0.99	$1.00/1.00 = 1.00$	±0.00	0.43
NGC 4214	...	...	...	...	...	...
NGC 4449	$0.27/0.23 = 1.17$	$+0.03$	0.02	$0.25/0.25 = 1.00$	$+0.06$	0.01
NGC 5253	$0.23/0.19 = 1.21$	$+0.01$	0.14	$0.20/0.21 = 0.95$	$+0.02$	0.07
He 2-10	$1.12/0.88 = 1.28$	-0.01	0.06	$1.00/0.97 = 1.03$	-0.01	0.31

Table 28. Improved fitted parameters for models (a) and (b) listed in Table 27

Method	(a)			(b)		
	$N_{\rm H}$	T	$Norm^a$	$N_{\rm H}$	T	$Norm^a$
	$[10^{21}\,{\rm cm}^{-2}]$	$[10^6\,{\rm K}]$	$[10^{-5}]$	$[10^{21}\,{\rm cm}^{-2}]$	$[10^6\,{\rm K}]$	$[10^{-5}]$
NGC 1569	1.67	7.07	63.95	2.14	7.04	112.9
NGC 3077	4.23	2.52	113.3	4.70	2.33	50.07
NGC 4214	11.15	1.92	1269	15.12	1.62	1188
NGC 4449	4.26	3.74	246.4	3.48	3.94	184.8
NGC 5253	3.15	4.28	40.98	3.04	4.31	41.71
He 2-10	0.00	7.06	1.04	0.15	7.03	8.63

X-ray luminosities of the diffuse component are in the range of $\sim 4 \times 10^{38} - 2 \times 10^{40}\,{\rm erg\ s}^{-1}$ and therefore span about two orders of magnitude. Absorbing column densities are in the range of $2 - 10 \times 10^{21}\,{\rm cm}^{-2}$.

- The metallicities of the hot gas cannot be reliably constrained but are compatible with the metallicities measured for H II regions. The α/Fe ratio is compatible with a value of ~ 2 (except for NGC 3077: $\alpha/Fe \sim 1$) which agrees with a scenario in which type II SNe are responsible for the ejected material stored in the superwinds.
- Azimuthally averaged X-ray surface brightness profiles are well described by exponential laws with scale lengths of $\sim 100 - 600$ pc. At large radii the profiles may level off. For most galaxies the scale length of the soft X-ray emission is larger than that of the hard emission.
- Fitted absorbing column densities are used to derive the orientation of the discs of the galaxies assuming that the soft X-rays are absorbed by the cooler gas stored in the discs.

In Paper II we present a comparison of the X-ray data with observations at other wavelengths, a discussion on the state of the ISM, correlations with star formation tracers, and the development of superwinds which can lead to outflows.

ACKNOWLEDGEMENTS

We would like to thank Dominik Bomans, John Cannon, Deidre Hunter, Chip Kobulnicky, and Vince McIntyre for providing optical and Hα images of the galaxies. In particular, we thank Crystal Martin for providing some optical images as well as for valuable discussions on NGC 3077 and He 2-10. We are also grateful to David Strickland for the critical reading of the manuscript. JO acknowledges generous support from the Graduiertenkolleg 118 'The Magellanic System, Galaxy Interaction, and the Evolution of Dwarf Galaxies' of the Deutsche Forschungsgemeinschaft (DFG). EB is grateful to CONACyT for financial support through grant Nr. 27606-E. This research has made use of the NASA/IPAC Extragalactic Database (NED) and the NASA/IPAC Infrared Science Archive, which are maintained by the Jet Propulsion Laboratory, Caltech, under contract with the National Aeronautics and Space Administration (NASA), NASA's Astrophysical Data System Abstract Service (ADS), NASA's SkyView, and the astronomical database SIMBAD, provided by the 'Centre de Données astronomiques de Strasbourg' (CDS).

REFERENCES

Anders E., Grevesse N. 1989, Geochim. Cosmochim. Acta, 53, 197
Balucinska–Church M., McCammon D. 1992, ApJ, 400, 699
Bi H. G., Arp H., Zimmermann H. U. 1994, A&A, 282, 386
Bignell R. C., Seaquist E. R. 1983, ApJ, 270, 140
Blair, W. P. & Long, K. S. 2004, ApJS, 155, 101
Blair W. P., Kirshner R. P., Winkler P. F. 1983, ApJ, 272, 84
Bomans D. J., Weis K., 2002, in The High Energy Universe at Sharp Focus: Chandra Science, eds. E. M. Schlegel & S. D. Vrtilek. San Francisco: ASP, 141
Bomans D. J. 2001, Ap&SS, 276, 783
Bomans D. J., Chu Y., Hopp U. 1997, AJ, 113, 1678
Cannon J. M., Skillman E. D., Garnett D. R., Dufour R. J. 2002, ApJ, 565, 931
Conti P. S. 1991, ApJ, 377, 115
della Ceca R., Griffiths R. E., Heckman T. M. 1997, ApJ, 485, 581
della Ceca R., Griffiths R. E., Heckman T. M., Lehnert M. D., Weaver K. A. 1999, ApJ, 514, 772
della Ceca R., Griffiths R. E., Heckman T. M., MacKenty J. W. 1996, ApJ, 469, 662
Fabbiano G., Feigelson E., Zamorani G. 1982, ApJ, 256, 397
Fabbiano G., Kim D.–W., Trinchieri G. 1992, ApJS, 80, 531
Ferland, G. J., Korista, K. T., Verner, D. A., Ferguson, J. W., Kingdon, J. B., & Verner, E. M. 1998, PASP, 110, 761
Ferrara A., Tolstoy E. 2000, MNRAS, 313, 291
Freedman W. L. et al. 1994, ApJ, 427, 628
Frei Z., Guhathakurta P., Gunn J. E., Tyson J. A. 1996, AJ, 111, 174
Gazol-Patiño, A. & Passot, T. 1999, ApJ, 518, 748
Gehrels N. 1986, ApJ, 303, 336
Gibson B. K. et al. 2000, ApJ, 529, 723
Guseva N. G., Izotov Y. I., Thuan T. X. 2000, ApJ, 531, 776
Hartman D. & Burton W. B. 1997, in Atlas of Galactic Neutral Hydrogen, (Cambridge: Cambridge University Press)
Hartwell J. M., Stevens I. R., Strickland D. K., Heckman T. M., Summers L. K., 2004, MNRAS, 348, 406
Heckman T. M. 2002, in ASP Conf. Ser. 254: Extragalactic Gas at Low Redshift, 292
Heckman T. M., Dahlem M., Lehnert M. D., Fabbiano G., Gilmore D., Waller W. H. 1995, ApJ, 448, 98
Hunter D. A., Hoffman L. 1999, AJ, 117, 2789
Hunter D. A., Wilcots E. M., van Woerden H., Gallagher J. S., Kohle S. 1998, ApJ, 495, L47
Irwin J. A., Athey A. E., Bregman J. N. 2003, ApJ, 587, 356
Israel F. P. 1988, A&A, 194, 24
Izotov Y. I., Thuan T. X., Lipovetsky V. A. 1997, ApJS, 108, 1
Kaastra J. S. 1992, An X–Ray Spectral Code for Optically Thin Plasmas (Internal SRON–Leiden Report updated version 2.0)
Kobulnicky H. A. Skillman E. D., 1996, ApJ, 471, 211
Kobulnicky H. A., Johnson K. E. 1999, ApJ, 527, 154
Kobulnicky H. A., Kennicutt R. C., Pizagno J. L. 1999, ApJ, 514, 544
Korpi M. J., Brandenburg A., Shukurov A., Tuominen I., Nordlund Å. 1999, ApJ, 514, L99
Lauberts A. & Valentijn E. A. 1989, Garching: European Southern Observatory
Legrand F., Tenorio–Tagle G., Silich S., Kunth D., Cerviño M. 2001, ApJ, 560, 630
Leitherer, C., Robert, C., & Drissen, L. 1992, ApJ, 401, 596
Liedahl D. A., Osterheld A. L., Goldstein W. H. 1995, ApJ, 438, L115
Lynds R., Tolstoy E., O'Neil E. J., Hunter D. A. 1998, AJ, 116, 146
Mac Low M., Ferrara A. 1999, ApJ, 513, 142
Maíz-Apellániz J., Cieza L., MacKenty J. W. 2002, AJ, 123, 1307
Martin C. L. 1996, ApJ, 465, 680
Martin C. L. 1997, ApJ, 491, 561
Martin C. L. 1998, ApJ, 506, 222
Martin C. L., Kennicutt R. C. 1995, ApJ, 447, 171
Martin C., Kobulnicky H., Heckman T. 2002, ApJ, 574, 663
Matteucci F., Recchi S. 2001, ApJ, 558, 351
McKee C. F., Ostriker J. P. 1977, ApJ, 218, 148
Meier D. S., Turner J. L., Beck S. C. 2002, AJ, 124, 877
Méndez D. I., Esteban C., Filipović M. D., Ehle M., Haberl F., Pietsch W., Haynes R. F. 1999, A&A, 349, 801
Mewe R., Gronenschild E. H. B. M., van den Oord G. H. J. 1985, A&AS, 62, 197
Östlin G. 2000, ApJ, 535, L99
Ott J., Walter F., Brinks E. 2004, MNRAS, submitted (**Paper II**)
Ott J., Martin C. L., Walter F. 2003, ApJ, 594, 776
Papaderos P., Fricke K. J., Thuan T. X., Loose H.–H. 1994, A&A, 291, L13
Raymond J. C., Smith B. W. 1977, ApJS, 35, 419
Roberts T. P., Warwick R. S. 2000, MNRAS, 315, 98
Schaerer D., Contini T., Pindao M. 1999, A&AS, 136, 35
Silich S., Tenorio–Tagle G. 2001, ApJ, 552, 91
Silich S. A., Tenorio-Tagle G., Terlevich R., Terlevich E., Netzer H. 2001, MNRAS, 324, 191
Smith R. K., Brickhouse N. S., Liedahl D. A., Raymond J. C. 2001, ApJ, 556, L91
Stevens I. R., Strickland D. K. 1998, MNRAS, 294, 523
Strickland D. K., Heckman T. M., Weaver K. A., Hoopes C. G., Dahlem M. 2002, ApJ, 568, 689
Strickland D. K., Stevens I. R. 1999, MNRAS, 306, 43
Summers, L. K., Stevens, I. R., Strickland, D. K., & Heckman, T. M. 2004, MNRAS, 351, 1
Summers L. K., Stevens I. R., Strickland D. K., Heckman T. M., 2003, MNRAS, 342, 690
Sutherland R. S., Dopita M. A. 1993, ApJS, 88, 253
Thuan, T. X., Bauer, F. E., Papaderos, P., & Izotov, Y. I. 2004, ApJ, 606, 213
Tozzi P., et al., 2001, ApJ, 562, 42
Vacca W. D., Conti P. S. 1992, ApJ, 401, 543
Vogler A., Pietsch W. 1997, A&A, 319, 459
Wada, K., Spaans, M., & Kim, S. 2000, ApJ, 540, 797
Walter F., Taylor C. L., Hüttemeister S., Scoville N., McIntyre V. 2001, AJ, 121, 727

Walter F., Weiss A., Martin C., Scoville N. 2002, AJ, 123, 225
Weaver R., McCray R., Castor J., Shapiro P., Moore R. 1977, ApJ, 218, 377

This paper has been typeset from a TEX/ LATEX file prepared by the author.